TECHNICAL REPORT

https://doi.org/10.1038/s41593-021-00841-5





Multimodal neural recordings with Neuro-FITM uncover diverse patterns of cortical-hippocampal interactions

Xin Liu^{1,7}, Chi Ren^{2,3,4,7}, Yichen Lu^{1,7}, Yixiu Liu¹, Jeong-Hoon Kim¹, Stefan Leutgeb^{2,3,5}, Takaki Komiyama^{2,3,4,6 ⋈} and Duygu Kuzum^{1,6 ⋈}

Many cognitive processes require communication between the neocortex and the hippocampus. However, coordination between large-scale cortical dynamics and hippocampal activity is not well understood, partially due to the difficulty in simultaneously recording from those regions. In the present study, we developed a flexible, insertable and transparent microelectrode array (Neuro-FITM) that enables investigation of cortical-hippocampal coordinations during hippocampal sharp-wave ripples (SWRs). Flexibility and transparency of Neuro-FITM allow simultaneous recordings of local field potentials and neural spiking from the hippocampus during wide-field calcium imaging. These experiments revealed that diverse cortical activity patterns accompanied SWRs and, in most cases, cortical activation preceded hippocampal SWRs. We demonstrated that, during SWRs, different hippocampal neural population activity was associated with distinct cortical activity patterns. These results suggest that hippocampus and large-scale cortical activity interact in a selective and diverse manner during SWRs underlying various cognitive functions. Our technology can be broadly applied to comprehensive investigations of interactions between the cortex and other subcortical structures.

rain computations often require interactions between different cortical and subcortical structures. Understanding of these long-range interactions in the brain requires monitoring of simultaneous activity patterns across these areas. This could be achieved by simultaneous multimodal recordings combining electrophysiological recordings and large-scale functional optical imaging. However, seamless integration of optical imaging with electrophysiology is difficult with conventional microelectrodes because large probe shanks made of rigid and opaque materials can prevent lowering of the microscope objective and block the field of view of imaging. To address this issue, we developed 'Neuro-FITM', an array that can be implanted into deep cortical layers and subcortical structures. The flexible probe shank of Neuro-FITM can be bent to the side to allow lowering of the microscope objective. Optical transparency of the shank provides a clear field of view and prevents optical shadows or additional noise in optical signals. Low impedance of Neuro-FITM provides reliable recordings of local field potentials (LFPs), high-frequency oscillations and single units with a high signal-to-noise ratio (SNR).

In the present study, we performed multimodal experiments with Neuro-FITM to investigate the coupling between the hippocampus and the cortex during SWRs. It has been suggested that hippocampal SWRs coordinate activity between the hippocampus and the cortex¹⁻⁴. Experiments with closed-loop manipulations have shown the indispensable role of SWRs in learning and memory⁵⁻⁷. However, most studies focused only on a single or a few cortical regions⁸⁻¹², so little is known about the simultaneous interaction between multiple cortical regions and the hippocampus during SWRs. Furthermore,

it is unclear whether the cortex is passively activated by hippocampal SWRs or whether certain cortical activity patterns can precede SWRs. Importantly, simultaneous variations across SWRs in hippocampal population activity and cortical activity patterns have not been studied. These questions could be addressed by simultaneous multimodal recordings that include electrophysiological recordings of the hippocampus and functional imaging of the cortex across large areas. We implanted Neuro-FITM into the hippocampus and performed simultaneous electrophysiological recordings of SWRs and single units during wide-field calcium imaging of most of the dorsal cortex in awake, head-fixed mice. Empowered by the multimodal recording capability, we investigated the large-scale cortical activity patterns associated with SWRs on a single-event basis using tensor component analysis (TCA)¹³ and found a rich spatiotemporal diversity. Furthermore, by performing decoding analysis with a support vector machine (SVM)14, we found that different cortical activity patterns relate to distinct activity of hippocampal neurons. Our results reveal that SWRs accompany diverse and specific interactions between the activity of the hippocampus and that of the cortex, and support the model that SWRs mediate diverse cortical-hippocampal interactions depending on the behavioral context and demand.

Results

Neuro-FITM fabrication and characterization. Neuro-FITM arrays developed in the present study combine three key advantages: flexibility, transparency and shuttle-free implantation in a single probe. They were fabricated on transparent and flexible

¹Department of Electrical and Computer Engineering, University of California San Diego, La Jolla, CA, USA. ²Neurobiology Section, Division of Biological Sciences, University of California San Diego, La Jolla, CA, USA. ³Center for Neural Circuits and Behavior, University of California San Diego, La Jolla, CA, USA. ⁴Department of Neurosciences, University of California San Diego, La Jolla, CA, USA. ⁵Kavli Institute for Brain and Mind, University of California San Diego, La Jolla, CA, USA. ⁶Halıcıoğlu Data Science Institute, University of California San Diego, La Jolla, CA, USA. ⁷These authors contributed equally: Xin Liu, Chi Ren, Yichen Lu. [∞]e-mail: tkomiyama@ucsd.edu; dkuzum@eng.ucsd.edu

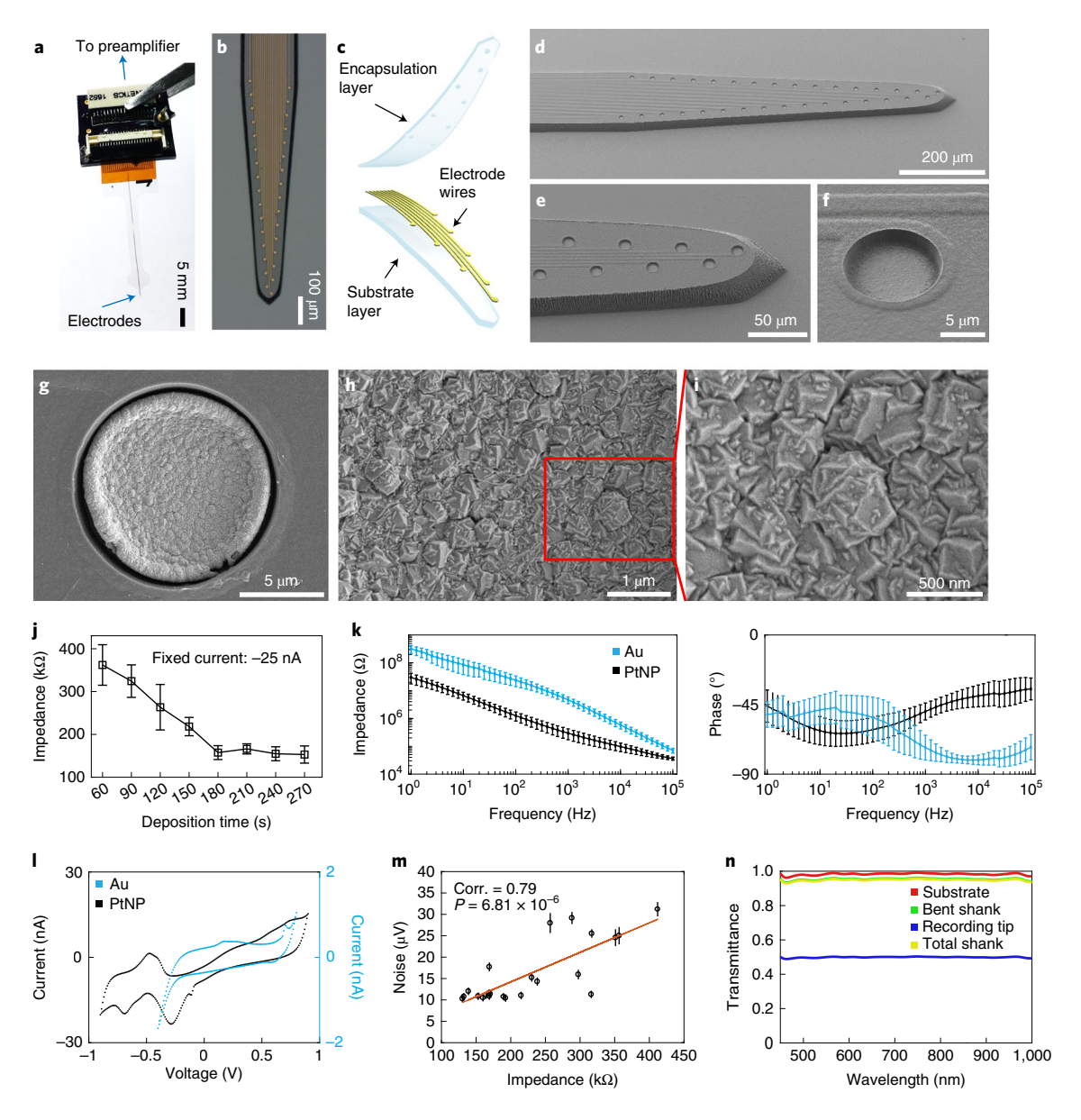


Fig. 1 | Characterization of Neuro-FITM. a, Neuro-FITM connected to the customized printed circuit board. b, Microscope image showing the layout of the microelectrode array. c, Schematic showing exploded view of the three-layered structure of Neuro-FITM. d-f, SEM images of the array showing 10-µm-diameter microelectrode openings and 2-µm-wide wires connecting to the microelectrodes: array tip showing the arrangement of microelectrodes (d); 10-µm-diameter microelectrodes and 2-µm-wide wires encapsulated with 2-µm-thick Parylene-C (e), and magnified view of a single microelectrode and its connected wires encapsulated with 2-µm-thick Parylene-C (f). g-i, SEM images showing PtNPs deposited on to the Au microelectrodes: PtNPs deposited on Au microelectrode (g) and surface and grains of PtNPs (h, and further magnified view in i). j, Electrode impedance as a function of deposition time during PtNP deposition (mean \pm s.d., n=3 electrodes for a deposition time of 60, 90, 180, 210 and 270 s; n=4 electrodes for 120, 150 and 240 s of deposition time). k, EIS magnitude (left) and phase (right) compared between Au and PtNP-deposited Au electrodes. PtNPs reduced the impedance of Au electrodes. The phase plot shows that PtNP electrodes are more resistive at higher frequency ranges than Au electrodes, consistent with the reduction in the impedance magnitude (mean \pm s.d., n = 26 electrodes for Au and n = 21 electrodes for PtNP). I, Cyclic voltammetry characteristics of PtNP-deposited electrodes showing redox peaks corresponding to electrochemical reactions of Pt, indicating an active engagement of PtNPs in the redox processes at the electrochemical interface. m, Noise level for electrodes with different impedances measured in 0.1M phosphate-buffered saline solution. Recorded signals were first high-pass filtered at 5 Hz and chunked into nonoverlapping 1-s segments. The noise level for each segment was defined as its root mean square value. Each dot marks the mean noise level for each recording channel. The error bar marks the s.e.m. for n = 87 measurements. The noise levels are higher for electrodes with higher impedance (two-sided Student's t-test, $P = 6.81 \times 10^{-6}$, n = 23, degree of freedom = 21). Corr., correlation. **n**, Transmittance of the substrate, the bent shank, the recording tip and the total shank as a function of wavelength.

Parylene-C substrate (Fig. 1a-c). Briefly, a polydimethylglutarimide sacrificial layer was spin-coated on a silicon wafer. A 14-µm-thick Parylene-C layer was deposited with the chemical-vapor deposition method. Then, 5-nm Cr and 100-nm Au were deposited with sputtering and patterned with photolithography and wet etching.

A 2-µm-thick Parylene-C layer was deposited as the encapsulation layer (Fig. 1c). Electrode openings were patterned with photolithography and oxygen plasma etching. The profile of the probe was defined with photolithography and oxygen reactive ion etching (Fig. 1d-f). Neuro-FITM arrays can be fabricated in various

configurations depending on the specific needs of the experiments. The Neuro-FITM probe shown in Fig. 1 is designed to record hippocampal LFPs and units during optical imaging. The width of the array is 50 μm at the tip, whereas the shank is tapered up to a maximum width of 170 μm at the top. The array consists of 32 circular recording electrodes, each with a diameter of 10 μm connected to 2- μm -wide wires. The scanning electron microscope (SEM) images show the profile of the probe and well-defined electrode openings (Fig. 1d–f). We fabricated several different configurations of Neuro-FITM, including probes with smaller electrode spacing (20 μm) for potential use in a tetrode configuration (Extended Data Fig. 1a), probes with a higher channel count (64 channels per shank; Extended Data Fig. 1b), and probes with longer shanks to allow recording from deeper structures of the brain or to use in rats (Extended Data Fig. 1c) and primates (Extended Data Fig. 1d).

Reducing the electrode impedance is important to minimize the electrical noise, particularly for single-unit recordings¹⁵⁻¹⁷. To achieve low impedance, platinum nanoparticles (PtNPs) were deposited on to 10-µm Au electrodes of Neuro-FITM probes (Fig. 1g-i)17. The electrode impedance can be controlled as a function of PtNP deposition time (Fig. 1j) and the size of the PtNP increases as the deposition time increases¹⁷. The largest grains of PtNPs are about 500 nm in diameter for 180s of deposition time. Electrochemical impedance spectroscopy (EIS) results show that the impedance of the Neuro-FITM electrodes was reduced by ~16× (Fig. 1k) as a result of PtNP deposition. Cyclic voltammetry (CV) measurements confirm that the PtNPs are actively engaged in the redox processes at the electrochemical interface (Fig. 11). The impedance of our 10- μ m-diameter electrodes is ~150 k Ω at 1 kHz, similar to those of the Neuropixel probes $(\sim 150 \,\mathrm{k}\Omega)^{18}$ even though the surface area $(78.5 \,\mu\text{m}^2)$ is half the size (Neuropixel = $144 \,\mu\text{m}^2$). Considering the impedance is inversely proportional to the electrode area, the impedance of Neuro-FITM electrodes is effectively two times smaller than the Neuropixel probes. We investigated the effect of impedance reduction on recording noise. Figure 1m shows recorded electrical noise as a function of electrode impedance, varied by controlling PtNP deposition time. Neuro-FITM electrodes exhibit sufficiently low noise (10 µV) for reliable detection and sort-

Optical transparency is important for seamless integration of electrophysiological recordings and optical imaging in multimodal experiments^{16,19}. We characterized the optical transparency of Neuro-FITM. The transmittance of the bent shank is ~95.7% and the recording tip with dense Au electrodes and interconnects shows a transmittance of ~50% (Fig. 1n). It is important to point out that, although the Au electrodes and Au wires are not transparent, the functional imaging would not be affected because: (1) Neuro-FITM is vertically implanted so that the penetrating tip of the probe does not directly block the light pathway and (2) the bent shank in the light pathway has thin Au wires, resulting in a high transmittance of ~95.7%. To better clarify the advantages of Neuro-FITM in multimodal configurations involving two-photon microscopy or wide-field imaging, we compared Neuro-FITM with commercially available NeuroNexus and Neuropixel probes (Extended Data Fig. 2). The high flexibility of Neuro-FITM allows bending of the probe shank away to lower the microscope objective for two-photon imaging (Extended Data Fig. 2b), whereas the rigid shanks of the Neuropixel and NeuroNexus probes prevent lowering of the microscope objective to its working distance. Wide-field microscope images (Extended Data Fig. 2c) show that NeuroNexus and Neuropixel probes block the field of view and generate shadows. In addition, large probe shanks can also result in out-of-focus images (Extended Data Fig. 2c, Neuropixel probe). Transparency of Neuro-FITM prevents blocking of the field of view and the formation of optical shadows that can obscure imaging. In addition to multiphoton imaging and wide-field imaging, the Neuro-FITM

array is also compatible with other optical imaging techniques commonly used in neuroscience, including near-infrared spectroscopy and diffuse optical tomography.

In vivo multimodal recordings with Neuro-FITM. Vertical implantation of Neuro-FITM arrays is critical for not blocking the light pathway during optical imaging and minimizing implantation damage. To implant Neuro-FITM arrays vertically without using a rigid shuttle or adding a bioresorbable stiffening layer, we carefully engineered the geometry and length of the microelectrode array by performing mechanical analysis to prevent buckling during insertion. Furthermore, the probe was designed to include additional micromanipulator pads to maximize insertion force against buckling (Fig. 2a; see Methods). Note that implantation of Neuro-FITM arrays with very long probe lengths designed for primate use (Extended Data Fig. 1d) will require the aid of shuttles during the insertion step. After the insertion and successful targeting of the hippocampus (Fig. 2b), the shank of the array was bent away to the side to allow lowering of the microscope objective to its working distance and to clear the field of view of the microscope (Fig. 2a and Extended Data Fig. 3a). The 2-µm-wide wires are confined to a narrow width to increase transparency of the shank and to minimize formation of shadows during imaging (Fig. 2c). To investigate the use of Neuro-FITM in in vivo multimodal experiments, we implanted it into the CA1 layer of hippocampus (Fig. 2b and Extended Data Fig. 3b) of transgenic mice expressing GCaMP6s in most cortical excitatory neurons²⁰ (CaMK2-tTA::tetO-GCaMP6s; see Methods). We performed simultaneous electrophysiological recordings of CA1 and wide-field calcium imaging of the dorsal cortex²¹. Hippocampal SWRs were detected in multiple channels located near the CA1 pyramidal layer (Fig. 2d), with concurrent large-scale cortical dynamics monitored using wide-field calcium imaging. Figure 2e shows representative examples of various spatial patterns of cortical activation during individual SWRs.

In addition to recordings of high-frequency SWR events, Neuro-FITM electrodes also detected spikes from multiple hippocampal neurons (12 ± 2 (mean \pm s.e.m.) neurons in each animal). Most neurons could be detected in multiple adjacent channels, each exhibiting different spike amplitudes (Extended Data Fig. 3c). Figure 3a shows spike waveforms of 21 neurons recorded across different channels in three recording sessions from one animal. Figure 3b shows the spike waveforms of all 21 neurons from the channel with the largest amplitude. Recorded neurons show stable spike waveforms across the sessions. The SNR of the electrical recordings is critical for spike detection and sorting as well as reliable detection of SWRs across different sessions. Therefore, we investigated the SNR for both unit (Fig. 4a) and LFP recordings, adopting the method used for measuring spike SNR of Neuropixel probes¹⁸. The SNR is computed as $A/(0.6457 \times B)$, where A is the maximum signal amplitude and *B* is the baseline taken as the median absolute deviation (MAD). The mean SNR of detected spikes is between 6 and 15 (Fig. 4b), similar to the SNR recorded by Neuropixel and other Si probes^{18,22}. To quantify the SNR of the LFP recordings, we measured the SNR for ripples and sharp-wave events using the same method¹⁸. The LFP signals recorded from the channels located in the pyramidal layer were bandpass filtered at the ripple frequency range (120-250 Hz) and sharp-wave frequency range (5-50 Hz), respectively. The baseline was then chosen as the MAD of the filtered signal from each channel. For each ripple event, the maximum signal amplitude is taken. The distribution of the detected amplitude and the SNR for ripples and sharp waves are shown in Fig. 4c,d-f, respectively. These results confirm that Neuro-FITM achieves high SNR for both single-unit and LFP recordings in all animals. Another important question is how the SNR of fluorescence response in wide-field imaging would be affected by the presence of Neuro-FITM electrodes. We characterized the SNR of the $\Delta F/F$ to quantify whether

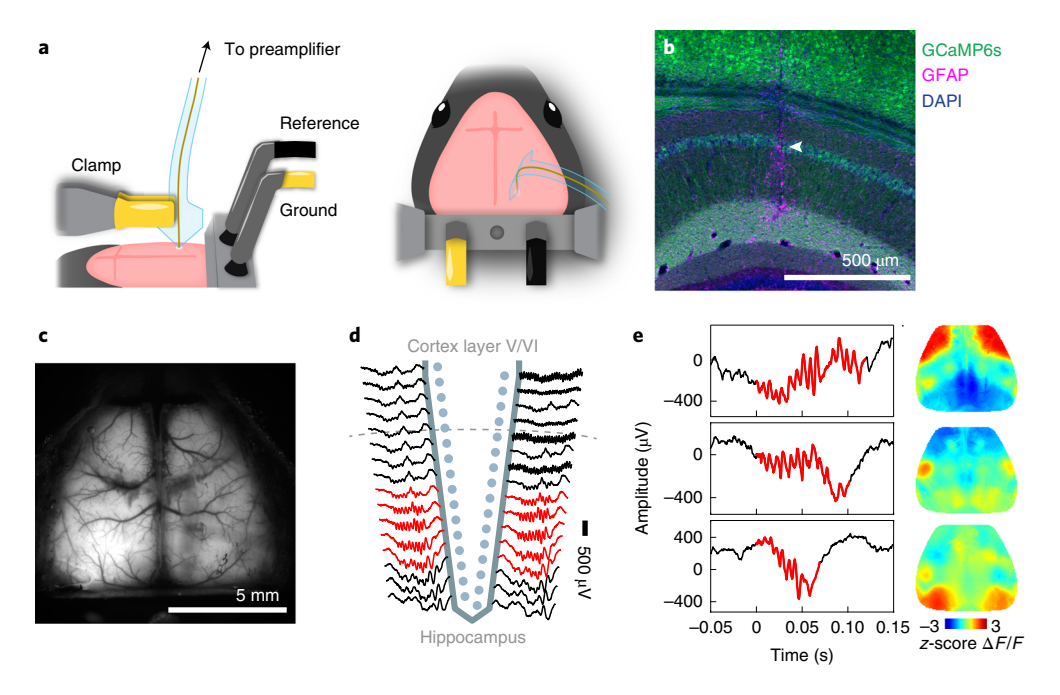


Fig. 2 | Simultaneous multimodal recordings from the hippocampus and cortex. a, Surgical setup. Neuro-FITM was first inserted into the hippocampus (left) and then the shank was bent down to the right side to allow lowering of the microscope objective and clearing of the field of view for imaging (right).
b, Penetrating trajectory of Neuro-FITM in the hippocampus visualized by immunostaining against GFAP. The arrowhead indicates the trajectory in the CA1 pyramidal layer. c, Field of view of wide-field calcium imaging during the experiment. Note that the array shank was largely invisible and generated minimal shadows on the overlaying cortex. d, Representative LFP recordings from the channels of the Neuro-FITM probe in one recording session. Multiple channels adjacent (red) to the pyramidal layer of CA1 detected SWRs. e, Examples of simultaneously recorded hippocampal SWRs (left column) and cortical activity (right column, single image frames at SWR onset). Cortical activity shows diverse spatial patterns during SWRs.

the implanted array affects imaging quality following the procedure used in a previous study²³. Briefly, we first identified the onset and offset time points of each cortical activation event. The SNR of each event is computed as the ratio between the maximum $\Delta F/F$ amplitude during activation and the s.d. of the $\Delta F/F$ fluctuation during [–1 s, 0 s] before onset. We found similar SNR for the fluorescence activity from the area covered by the Neuro-FITM shank and the corresponding area in the contralateral hemisphere (Fig. 4g), showing that Neuro-FITM does not significantly change the SNR of fluorescence signals during wide-field calcium imaging.

Cortical activation onset tends to precede hippocampal SWRs. Our multimodal recording setup with Neuro-FITM provides an ideal platform to investigate the spatiotemporal properties of cortical-hippocampal interactions during SWRs. We first examined the large-scale cortical activity patterns averaged across all SWRs. To analyze the onsets of cortical activity and SWR accurately without contamination from prior SWR events, we focused on SWRs that did not have other SWRs for at least the preceding 3 s (4,290 'well-separated SWRs' out of 8,643 SWRs). We found that the onset of cortical activation averaged across SWRs preceded SWR onset by 1.33 ± 0.15 s (mean \pm s.d.; Fig. 5a and Extended Data Fig. 4a) whereas the peak of cortical activation occurred $0.67 \pm 0.18 \,\mathrm{s}$ (mean ± s.d.) after the SWR onset. To investigate whether different cortical regions have different activation timing relative to SWR onset, we parcellated the dorsal cortex into 16 individual regions based on Allen Brain Atlas (Fig. 5b) and examined the activity of each cortical region around SWR onset. On average, all the cortical regions increased their activity around SWRs (Fig. 5c and Extended Data Fig. 4b). Furthermore, the activation onset timing of cortical regions relative to the SWR onset exhibited an anteroposterior gradient, with the earlier activation of posterior cortical regions such as visual cortex, retrosplenial cortex and posterior parietal cortex (Fig. 5d and Extended Data Fig. 5). Similarly, the fraction of SWR events with the activation of the cortical region leading SWR onset increased from anterior to posterior cortical regions (Fig. 5e). Of SWRs, 93.78% had at least one cortical region with activity onset preceding the SWR onset. Taken together, in most SWR events, the cortical activation started before hippocampal SWRs, especially in posterior cortical regions.

Distinct patterns of cortical activity around SWRs. Given that multimodal recordings with Neuro-FITM showed spatiotemporal variations in cortical activity from SWR event to SWR event (Fig. 2e), we next asked whether there were distinct cortical activation patterns that were reproducibly observed across subsets of the SWRs. Simultaneous wide-field imaging of the dorsal cortex and SWR recordings from the hippocampus with Neuro-FITM across many sessions generated large-scale neural datasets that can be analyzed to answer this question. To this end, we performed a two-stage TCA¹³ on the activity from all the recorded cortical regions during all SWR events, including SWRs that were and were not well separated. TCA is an unsupervised dimensionality reduction method that extracts recurring patterns in high-dimensional data (Extended Data Fig. 6) by decomposing the data into three factors (Fig. 6a). The region factors and time factors describe the spatial and temporal dynamics of cortical patterns, respectively, and the event factors measure the weighting of a given SWR event on the established set of patterns. By multiplying the region factors and time factors, we identified eight distinct cortical activity pattern templates that were common across all animals (Fig. 6b and Extended Data Fig. 7a). The patterns exhibited distinct activated regions focusing on either the anterior or the posterior cortices, with patterns 1, 2 and 3 dominated by anterior regions ('anterior patterns') and patterns 4, 5 and 6 dominated by posterior regions ('posterior patterns'), with different time courses relative to the SWR onset. Besides patterns 1-6

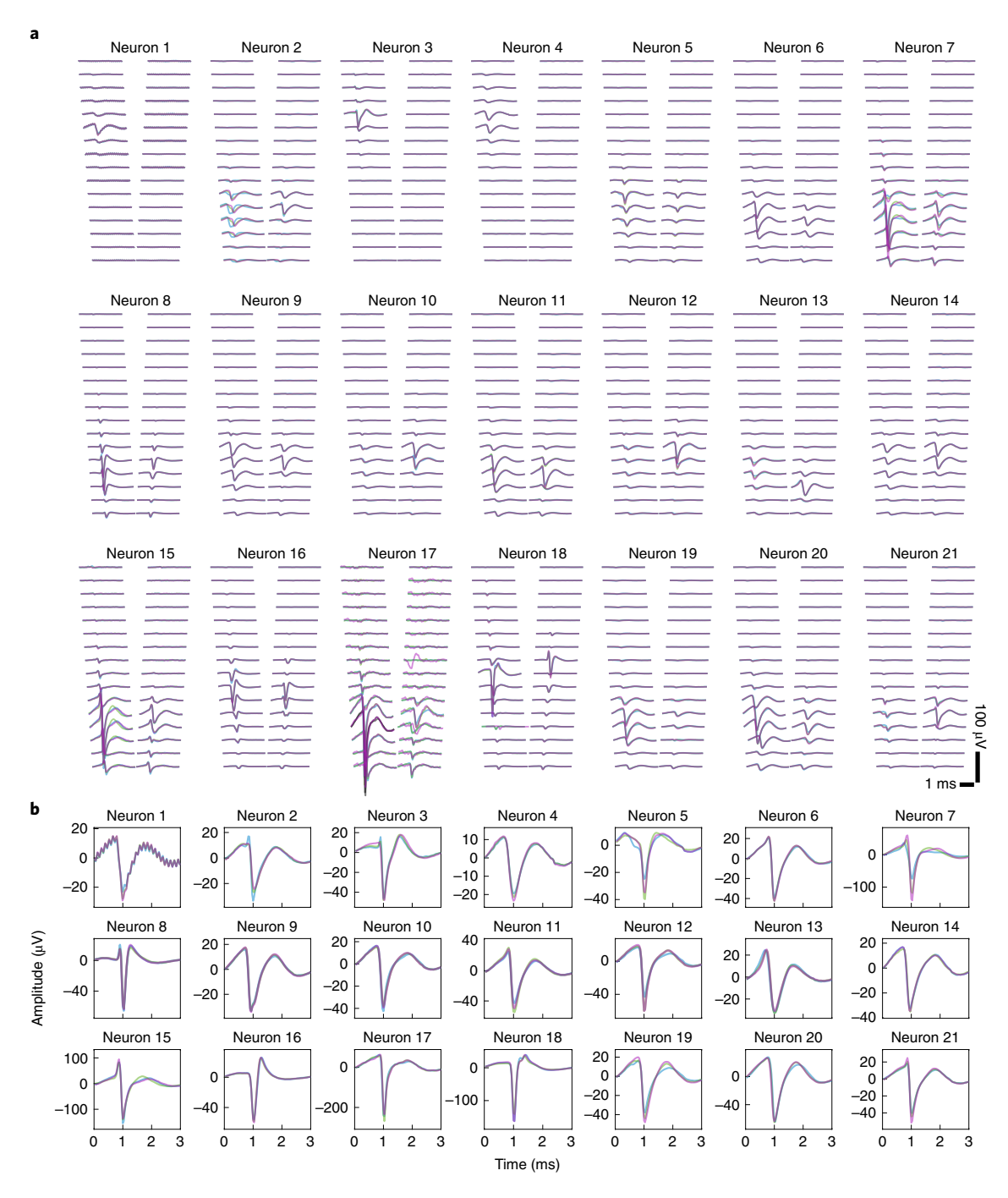


Fig. 3 | The neuron spike waveforms in different recording sessions from one mouse. a, Spatial profiles of spike waveforms of all 21 neurons recorded across 32 channels in three recording sessions marked by three different colors. Many neurons exhibit stable waveforms that are most prominent in adjacent channels. **b**, Spike waveforms of all 21 neurons from the channel with the largest amplitude recorded in three sessions. Different colors indicate different recording sessions, as in **a**. The waveforms of the same neuron recorded at different sessions are highly similar.

showing transient and spatially discrete activity patterns, pattern 7 was dominated by an extended activation in the visual cortex and pattern 8 showed periodic and oscillatory activation in all cortical regions. The cortical activity pattern in each SWR event could be well reconstructed as a linear sum of the eight templates weighted by the event factors (Extended Data Fig. 6b).

To explore the diversity of SWR-associated cortical activity, we first measured the two-dimensional (2D) correlation between the cortical activity during individual well-separated SWR events and each of the cortical pattern templates. The correlations for SWR

events followed a continuous distribution instead of aggregating into isolated clusters (Fig. 6c), indicating that broadly distributed diverse cortical activity patterns were associated with SWRs. To examine the SWR events with divergent associated cortical activity, we next focused our analysis on groups of SWR events with cortical activity that was mainly dominated by one of the cortical pattern templates (Fig. 6c, colored dots, 2D correlation >0.45). In total, ~36% of all the well-separated SWR events were assigned to one of the cortical pattern templates. The cortical activity averaged across the SWR events assigned to each cortical pattern template

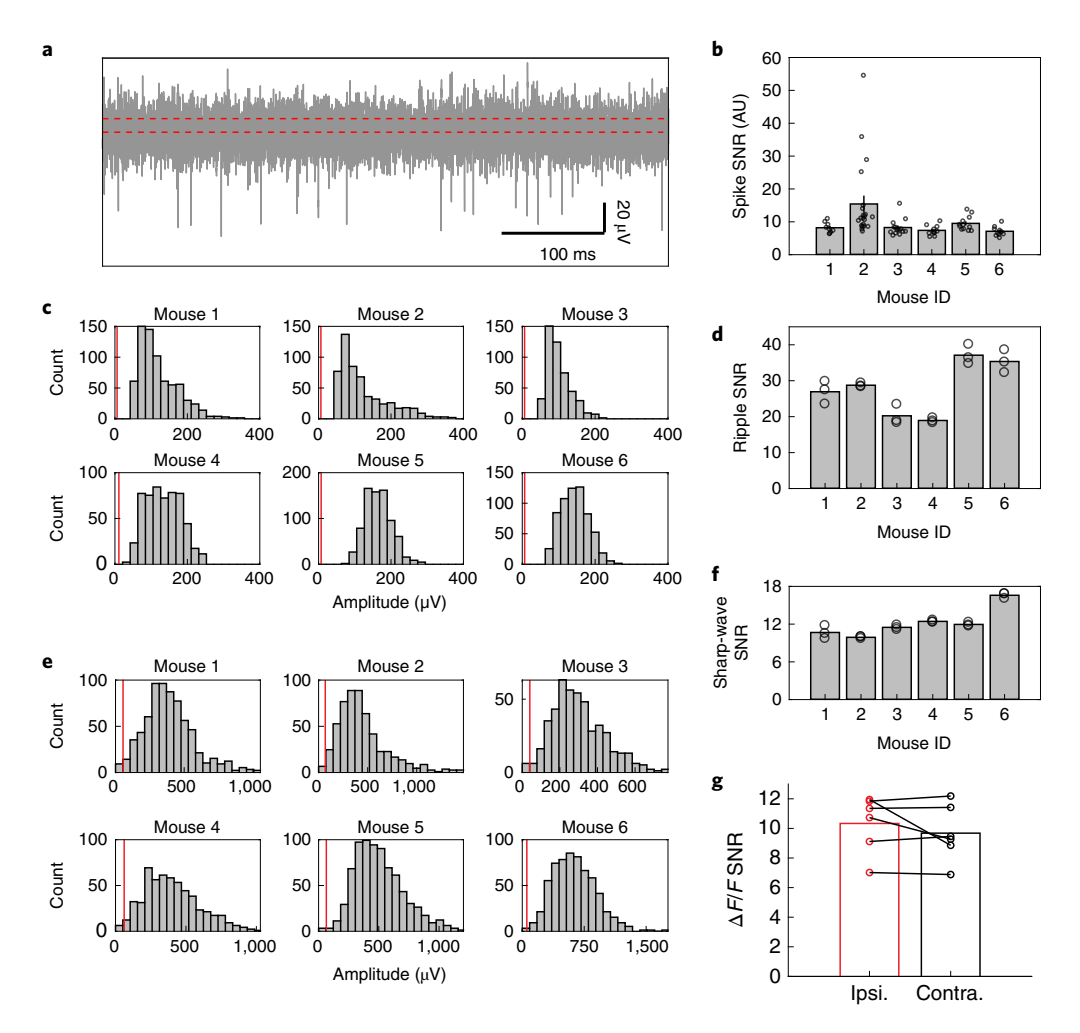


Fig. 4 | SNR for the spikes, LFPs and wide-field fluorescence. **a**, Representative example of high-pass-filtered data from one channel showing the detection of multiple spikes and the MAD denoted by the width between two red dashed lines. **b**, SNR of the recorded spikes in all six mice. The bar shows the mean SNR averaged over all the neurons and the error bar denotes the s.e.m. Each dot represents the spike SNR for one neuron. AU, arbitrary units. **c**, Histogram of amplitude of the detected ripples. The red line shows the MAD of the ripple-range LFPs (120–250 Hz). **d**, Mean SNR for the ripples detected in all six mice. Each dot represents the mean SNR of the ripples recorded in one recording channel. **e**, Histogram of amplitude of the sharp waves during SWR. The red line shows the MAD of the sharp-wave range LFPs (5–50 Hz). **f**, Mean SNR for the sharp waves detected in all six mice. Each dot represents the mean SNR of the sharp waves recorded in one recording channel. **g**, SNR of the $\Delta F/F$ for the cortical regions covered by the array shank (ipsilateral, Ipsi.) versus the symmetrical cortical regions on the contralateral (Contra.) side, showing a similar SNR for both cases.

highly resembled the corresponding template (Fig. 6d, compare with Fig. 6b). Thus, many SWR events accompany diverse sets of reproducible cortical activity patterns. For the SWR events assigned to the two patterns with peak activity immediately after ripple onset (patterns 2 and 5), we also found the activity onset of most cortical regions preceded ripple onset by 0.16–0.6s (Extended Data Fig. 7b). Figure 6e shows the fraction of SWR events assigned to each pattern for all the mice. Overall, there were more SWR events associated with the posterior cortical patterns than the anterior patterns, suggesting a more frequent coupling between the hippocampus and posterior cortical regions during SWRs.

Different cortical patterns associate with distinct hippocampal activity. Considering that SWR-associated cortical activity exhibited distinct patterns, we explored whether hippocampal neuronal activity during individual SWR events is differentially modulated depending on the concurrent cortical patterns. In addition to SWRs, Neuro-FITM electrodes also detect spikes from the nearby hippocampal neurons in multimodal experiments. Figure 7a shows three

representative hippocampal neurons exhibiting selective (neurons 1 and 2) or nonselective (neuron 3) firing rates at the onsets of SWRs associated with different cortical patterns. To study the distinct modulation of hippocampal neurons during different cortical activity patterns, we performed SVM decoding analysis to examine whether cortical patterns could be discriminated based on the hippocampal population activity. SVM is a decoding technique that looks for a hyperplane to best separate the data according to their classes, while maximizing the margin between the data samples and the hyperplane. SVM has been shown to give a robust decoding performance for high-dimensional data, especially when the size of the dataset is limited. As a result of this advantage, it has been commonly used to decode stimuli and choices using neuronal activity^{24–28}. In the present study, we built an SVM decoder that performs pairwise discrimination of cortical patterns based on hippocampal population activity. The SWR events associated with two cortical patterns were selected, and the decoder attempted to discriminate the cortical patterns using the spiking activity of the simultaneously recorded hippocampal neurons (12±2 neurons in each animal;

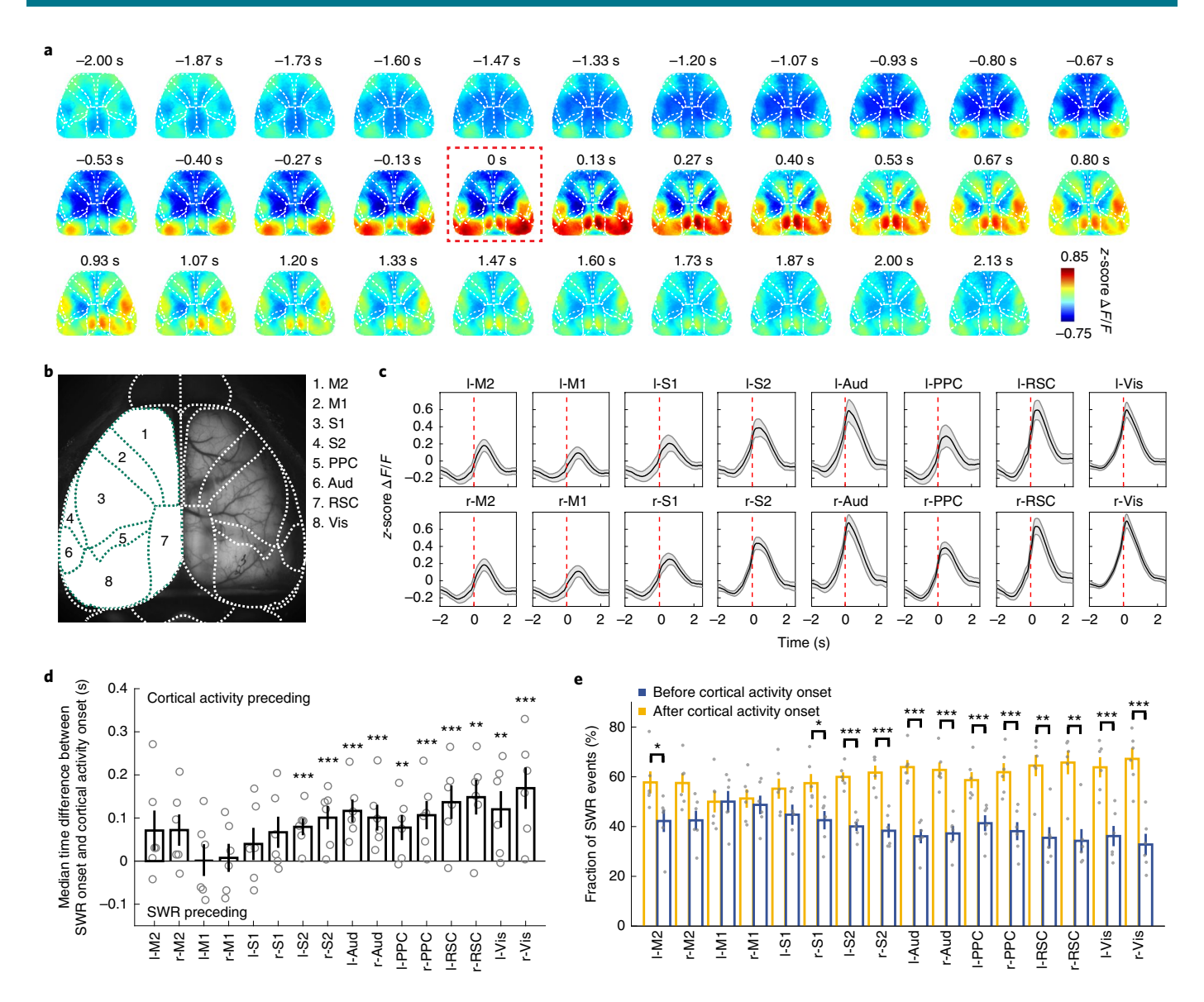


Fig. 7b). We used the recursive feature elimination algorithm²⁹, which selected the subset of neurons in each decoder with activity that was informative about the cortical activity patterns ('discriminant neurons'). This process was repeated for all pairs of cortical patterns. For many cortical pattern pairs, the cortical patterns could be discriminated significantly above chance based on the activity of hippocampal neurons during SWRs. Figure 7c shows the decoding accuracy for each cortical pattern pair from one example mouse. In all six mice, a large fraction of cortical pattern pairs was

distinguishable (Fig. 7d and Extended Data Fig. 8). By examining the decodable cortical pattern pairs, we found that different subsets of hippocampal neurons were discriminant for different cortical pattern pairs (Extended Data Fig. 9a), and all hippocampal neurons were discriminant in at least one of the pairs. These results suggest that all hippocampal neurons are modulated differently depending on cortical activity patterns during SWRs. We also repeated the decoding analysis using hippocampal pyramidal cells and interneurons separately. We found that both hippocampal pyramidal cells

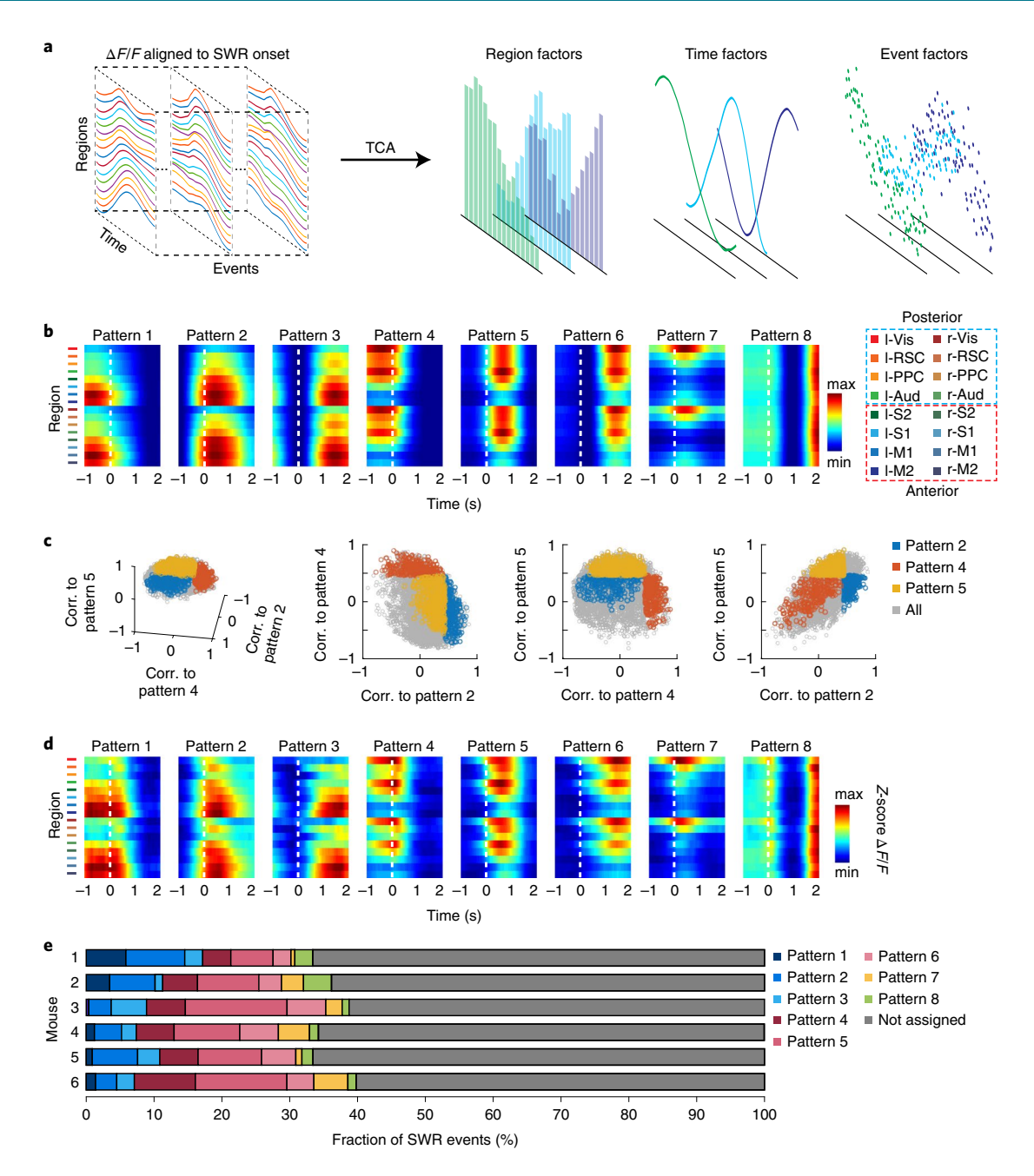


Fig. 6 | Diverse SWR-associated cortical activity patterns. a, Schematic of the TCA algorithm. The activity of 16 cortical regions during SWR events formed 3D tensors that were concatenated across mice. Using the two-stage TCA algorithm, the original data were decomposed into region, time and event factors to capture the spatiotemporal dynamics of single SWR events. **b**, Common SWR-associated cortical activity pattern templates identified across animals by the TCA algorithm. Note that patterns 1–6 exhibited activation of anterior or posterior cortical regions with three different time courses around SWR onsets. We defined patterns 1–3 as 'anterior patterns' and patterns 4–6 as 'posterior patterns' based on the activated cortical regions. Pattern 7 was dominated by an extended activation in the visual cortex and pattern 8 showed periodic activation in all cortical regions. Abbreviations as in Fig. 5b. **c**, Correlations (Corr.) of cortical activity from single SWR events with three of the cortical activity templates. Cortical activity during single SWR events showed a continuous distribution. **d**, SWR events, the cortical activity of which was dominated by single cortical pattern templates, were grouped separately (see text). The figure shows the average cortical activity during SWR events assigned to each template, which closely resembled the identified cortical activity templates shown in **b**. **e**, Fraction of SWR events assigned to each cortical pattern template for all six animals. More SWR events were assigned to posterior patterns (patterns 4–6) than anterior patterns (patterns 1–3), suggesting that the posterior regions associate with SWRs more frequently than anterior regions.

and interneurons can decode the cortical activity pattern, indicating that both neuron types were modulated specifically during SWRs (Extended Data Fig. 9b).

Given that many cortical pattern pairs could be decoded, we further investigated whether hippocampal neuron activity exhibited consistent modulations based on the different features of cortical activity patterns. To address this issue, we analyzed two groups of pattern pairs. One included pattern pairs with the same activation time course but different activated regions (anterior versus posterior, pattern 1 versus 4, 2 versus 5 and 3 versus 6), whereas the other

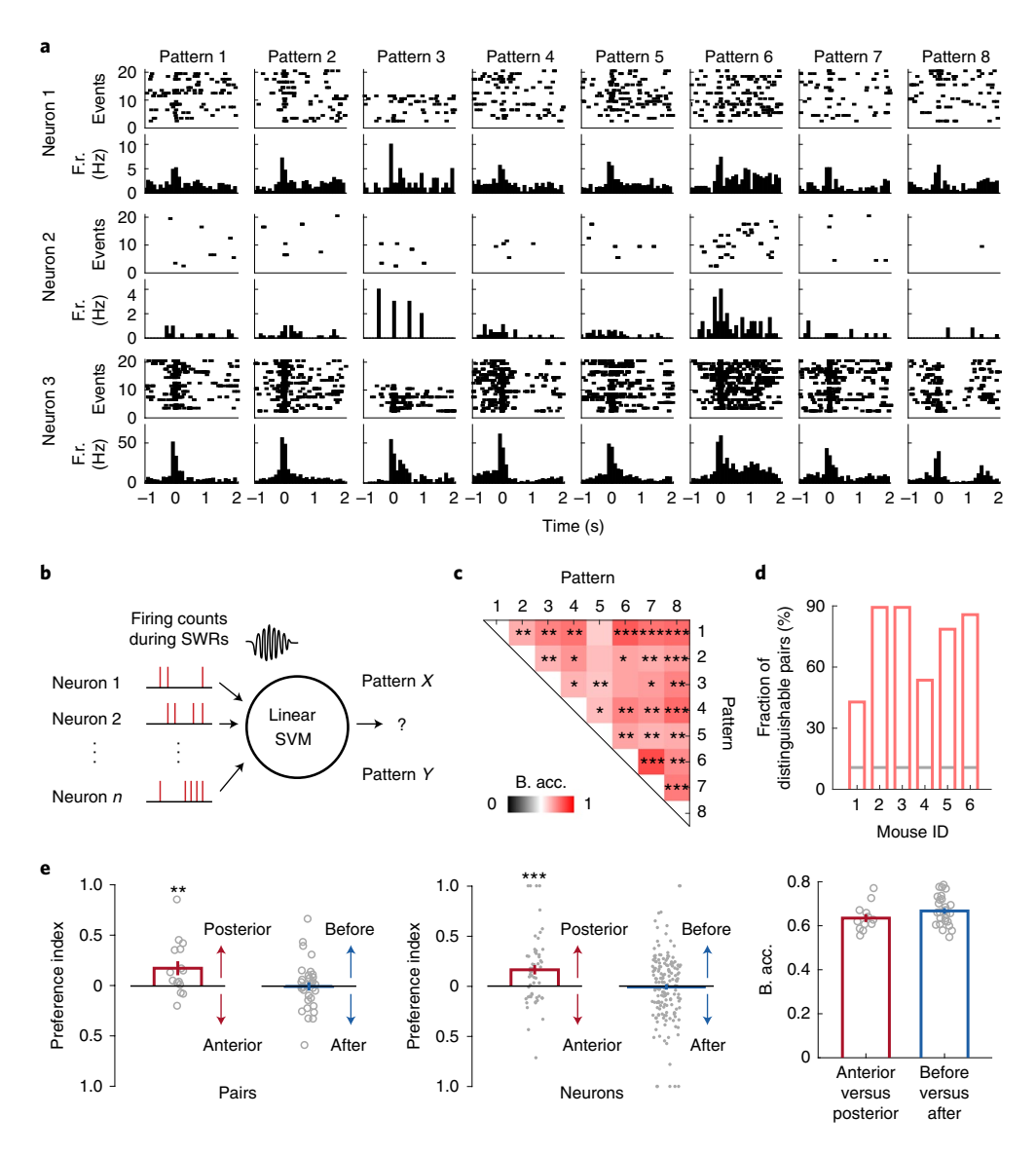


Fig. 7 | Different cortical activity patterns associated with distinct hippocampal neuronal activity patterns during SWRs. a, Raster plots (spikes) and the peri-event time histograms of example hippocampal neurons, showing different (neurons 1 and 2) and similar (neuron 3) firing rates at SWR onset under different cortical activity patterns. F.r., firing rate. b, Schematic of the decoding model. The firing counts of each hippocampal neuron during 0-100 ms relative to SWR onset were used as input features for the linear SVM to decode the cortical patterns. c, Decoding accuracy of all cortical pattern pairs from one example animal (mouse 2). Cortical pattern pairs that are significantly distinguishable based on hippocampal activity are marked by asterisks (shuffled 2,000 times, one tailed, $^*P < 0.05$, $^{**}P < 0.01$, $^{**}P < 0.001$; see Methods for exact P values). B. acc., balanced accuracy. **d**, Fraction of distinguishable cortical pattern pairs in each animal. Across six animals, many cortical pattern pairs were distinguishable based on the hippocampal neuron activity. The gray lines indicate the chance level fraction with P < 0.05 (one-sided binomial test, n = 28 pattern pairs). The P values for mice 1-6 are 2.24×10^{-10} , 5.10×10^{-32} , 5.10×10^{-32} , 2.60×10^{-14} , 9.17×10^{-26} and 8.42×10^{-30} . **e**, Preference index and decoding accuracy between anterior (A)-posterior (P) and early (E)-late (L) pattern pairs. Left: preference index of discriminant hippocampal neurons between A-P pairs (pattern 1 versus 4, 2 versus 5 and 3 versus 6) or between E-L patterns (pattern 1 versus 2, 1 versus 3, 2 versus 5, 4 versus 5, 4 versus 6 and 5 versus 6). Posterior patterns were associated with higher firing counts of discriminant neurons than the anterior patterns (two-tailed bootstrap test, 10,000 times, **P(A-P) = 0.0017, n = 15 pattern pairs) whereas no significant differences were detected between early and late patterns (P(E-L) = 0.4646, n = 33 pattern pairs). The gray circles indicate preference index averaged over all neurons for each pair within each animal. Middle: same as left but for individual discriminant neurons (two-tailed bootstrap test, 10,000 times, ***P(A-P) = 0.0001, n = 56 neurons; P(E-L) = 0.3802, n = 160 neurons). The gray dots indicate preference index of individual discriminant neurons. Right: decoding accuracy between A-P and E-L pairs was similar (two-tailed bootstrap test, 10,000 times, P = 0.0656, n = 15 pattern pairs for A-P, n = 33 pattern pairs for E-L). All error bars are s.e.m. The gray circles indicate decoding accuracy for each pair.

included pattern pairs with the same activated regions but different time courses (early versus late, for example, pattern 1 versus 2 or 4 versus 5). To compare the activation levels of discriminant neurons determined by the recursive feature elimination algorithm for cortical pattern pairs (Extended Data Fig. 9a), we defined the 'preference

index' for each neuron as the difference in the spike counts during one pattern versus the other, divided by the sum of the two (Methods). When comparing posterior with anterior patterns activated at similar timing, we found that posterior patterns were associated with higher firing in a majority of discriminant neurons than

the anterior patterns, which was evident in a significantly positive preference index (Fig. 7e). In contrast, when comparing cortical activation of similar areas but with different timing, the general activity level of discriminant neurons did not show a significant preference for earlier versus later activation (Fig. 7e). Despite the lack of consistent difference in the general hippocampal activation level for E-L pattern pairs, their decoding accuracy was similar to that for A-P pattern pairs (Fig. 7e). We also repeated the same decoding analysis and preference index analysis for all the ripple events, including the non-well-separated SWRs (Extended Data Fig. 10). The results are qualitatively similar compared with Fig. 7, indicating that the conclusions are generalizable across heterogeneous ripples. Taken together, these results reveal diverse associations between cortical activity patterns and hippocampal neuronal activity during SWRs. The posterior cortical activation is associated with stronger hippocampal activation in most of the hippocampal neurons. The relative timing between cortex and SWRs is associated with heterogeneous modulation of individual hippocampal neurons.

Discussion

We developed a mostly transparent, bendable microelectrode array (Neuro-FITM) to enable cortex-wide simultaneous optical imaging during electrophysiological recordings. To achieve the same goal, conventional silicon probes would have to be inserted contralaterally or horizontally, which would inevitably lead to long insertion trajectories causing additional implantation damage to the brain tissue. Furthermore, horizontal implantation will cause increased mechanical stress applied on to the thin silicon shank at the clamping point, which can lead to premature fracture of the probe. Instead, our flexible array could be inserted vertically to the hippocampus with the shortest trajectory, minimizing brain tissue damage. In addition, our Neuro-FITM has up to 64 recording electrodes per shank, providing a higher spatial resolution for electrophysiology compared with other polymer-based microelectrodes used for hippocampal recordings^{30,31}. Given the high flexibility and small dimensions of the insertable shank of the array, we anticipate that our flexible microelectrode array will improve the stability of unit recordings in chronic studies.

Our Neuro-FITM array could potentially be combined with other neural technologies that further expand its applications into various neuroscience studies. For example, Neuro-FITM array could be integrated with wireless electrophysiological recording platforms for wireless data transmission^{32–34}, which are ideal for recordings in freely moving animals. The Neuro-FITM array could also be augmented to allow simultaneous electrophysiological recordings and manipulations of neural activity. This could be achieved by optimizing the charge injection capacity of the electrodes for electrical stimulation³⁵, or by incorporating micro-light-emitting diodes³⁶ or waveguides³⁷ into the device to form optoelectronic neural interfaces.

The simultaneous multimodal recordings of the hippocampal and cortical activity allowed us to characterize the cortical-hippocampal interactions during individual SWRs. In contrast to the conventional notion that cortical activity is mainly triggered by hippocampal SWRs^{11,12,38-41} (but see refs. ^{8-10,42}), our findings suggest that the hippocampus and cortex exhibit bidirectional communications, with the cortical activation frequently preceding SWR onset. Furthermore, the relative timing between cortical activation and SWRs is area specific. The cortical activation could start before or after SWRs in both anterior and posterior cortical regions, whereas the activation of posterior cortical regions precedes SWRs more frequently than that of anterior regions. A previous study in nonhuman primates performed simultaneous functional magnetic resonance imaging (fMRI) recordings of the whole brain and electrophysiological recordings of the hippocampus, and showed that the activation of several cortical regions can, on average, precede

hippocampal SWRs. However, the SNR of fMRI limited their analysis to the average activity across SWRs and prevented the analysis of the diversity of cortical activity during individual SWRs⁴. The approach adopted in the present study achieved a sufficient SNR to perform single-event analyses across large recording areas to uncover the remarkable and coordinated diversity of cortical and hippocampal activity during SWRs. The activation of different cortical regions with different timing relative to SWR onset forms distinct cortical activity patterns from SWR to SWR. Importantly, these cortical activity patterns differentially associate with the hippocampal neuronal activity, which indicated that these patterns are not merely random fluctuation but that there is, rather, a predictable relationship of cortical activity patterns with hippocampal neuron populations, indicative of large-scale neuron assemblies that span the hippocampus and cortex.

The interaction between hippocampus and single brain regions under different behavioral states has been extensively studied. For example, it has been reported that awake SWRs were accompanied by the reactivation of neurons in the prefrontal cortex, suggesting that the awake SWRs played important roles in memory retrieval^{11,43}. On the other hand, the existence of a bidirectional loop between the hippocampus and the auditory cortex, which could play a role in memory consolidation, was also demonstrated9. A recent study showed that, on a larger scale, the coupling between hippocampal ripples and ripples in association cortices becomes stronger after spatial learning, suggesting a closer communication between the hippocampus and association cortices during memory transfer⁴⁴. The hippocampus encodes a variety of information including spatial, sensory and reward⁴⁵⁻⁴⁹. The broad and diverse activation of cortical regions we observed during hippocampal SWRs may reflect a specific binding of distinct types of information encoded in the hippocampus and the relevant cortical regions through different anatomical connections. The diversity of cortical-hippocampal interactions around SWRs suggests that the hippocampus and cortex can communicate through multiple information streams based on contexts and cognitive processes. Future studies should uncover how such cortical-hippocampal interaction is dynamically shaped when the animals are experiencing different task contexts or under different behavioral states.

Online content

Any methods, additional references, Nature Research reporting summaries, source data, extended data, supplementary information, acknowledgements, peer review information; details of author contributions and competing interests; and statements of data and code availability are available at https://doi.org/10.1038/s41593-021-00841-5.

Received: 23 January 2020; Accepted: 15 March 2021; Published online: 19 April 2021

References

- Skelin, I., Kilianski, S. & McNaughton, B. L. Hippocampal coupling with cortical and subcortical structures in the context of memory consolidation. *Neurobiol. Learn. Mem.* 160, 21–31 (2019).
- Buzsáki, G. Hippocampal sharp wave-ripple: a cognitive biomarker for episodic memory and planning. Hippocampus 25, 1073–1188 (2015).
- Todorova, R. & Zugaro, M. Hippocampal ripples as a mode of communication with cortical and subcortical areas. *Hippocampus* https://doi. org/10.1002/hipo.22997 (2018).
- Logothetis, N. K. et al. Hippocampal–cortical interaction during periods of subcortical silence. *Nature* 491, 547–553 (2012).
- Jadhav, S. P., Kemere, C., German, P. W. & Frank, L. M. Awake hippocampal sharp-wave ripples support spatial memory. Science 336, 1454–1458 (2012).
- Maingret, N., Girardeau, G., Todorova, R., Goutierre, M. & Zugaro, M. Hippocampo-cortical coupling mediates memory consolidation during sleep. Nat. Neurosci. 19, 959–964 (2016).
- Girardeau, G., Benchenane, K., Wiener, S. I., Buzsáki, G. & Zugaro, M. B Selective suppression of hippocampal ripples impairs spatial memory. Nat. Neurosci. 12, 1222–1223 (2009).

- Sirota, A., Csicsvari, J., Buhl, D. & Buzsáki, G. Communication between neocortex and hippocampus during sleep in rodents. *Proc. Natl Acad. Sci.* USA 100, 2065–2069 (2003).
- Rothschild, G., Eban, E. & Frank, L. M. A cortical-hippocampal-cortical loop of information processing during memory consolidation. *Nat. Neurosci.* 20, 251–259 (2017).
- Ji, D. & Wilson, M. A. Coordinated memory replay in the visual cortex and hippocampus during sleep. *Nat. Neurosci.* 10, 100–107 (2007).
- Jadhav, S. P., Rothschild, G., Roumis, D. K. & Frank, L. M. Coordinated excitation and inhibition of prefrontal ensembles during awake hippocampal sharp-wave ripple events. *Neuron* 90, 113–127 (2016).
- Chrobak, J. & Buzsáki, G. Selective activation of deep layer (V–VI) retrohippocampal cortical neurons during hippocampal sharp waves in the behaving rat. J. Neurosci. 14, 6160–6170 (1994).
- Williams, A. H. et al. Unsupervised discovery of demixed, low-dimensional neural dynamics across multiple timescales through tensor component analysis. *Neuron* 98, 1099–1115 (2018).
- Cortes, C. & Vapnik, V. Support-vector networks. *Mach. Learn.* 20, 273–297 (1995).
- Won, S. M. et al. Recent advances in materials, devices, and systems for neural interfaces. Adv. Mater. 30, 1800534 (2018).
- Thunemann, M. et al. Deep 2-photon imaging and artifact-free optogenetics through transparent graphene microelectrode arrays. *Nat. Commun.* 9, 2035 (2018).
- 17. Lu, Y. et al. Ultralow impedance graphene microelectrodes with high optical transparency for simultaneous deep two-photon imaging in transgenic mice. *Adv. Funct. Mater.* **28**, 1800002 (2018).
- Jun, J. J. et al. Fully integrated silicon probes for high-density recording of neural activity. Nature 551, 232–236 (2017).
- Kuzum, D. et al. Transparent and flexible low noise graphene electrodes for simultaneous electrophysiology and neuroimaging. *Nat. Commun.* 5, 5259 (2014).
- Wekselblatt, J. B., Flister, E. D., Piscopo, D. M. & Niell, C. M. Large-scale imaging of cortical dynamics during sensory perception and behavior. J. Neurophysiol. 115, 2852–2866 (2016).
- Makino, H. et al. Transformation of cortex-wide emergent properties during motor learning. Neuron 94, 880–890 (2017).
- Shobe, J. L., Claar, L. D., Parhami, S., Bakhurin, K. I. & Masmanidis, S. C. Brain activity mapping at multiple scales with silicon microprobes containing 1,024 electrodes. J. Neurophysiol. 114, 2043–2052 (2015).
- Yang, Y. et al. Improved calcium sensor GCaMP-X overcomes the calcium channel perturbations induced by the calmodulin in GCaMP. *Nat. Commun.* 9, 1–18 (2018).
- Chu, M. W., Li, W. L. & Komiyama, T. Balancing the robustness and efficiency of odor representations during learning. *Neuron* 92, 174–186 (2016).
- Cichy, R. M., Pantazis, D. & Oliva, A. Resolving human object recognition in space and time. Nat. Neurosci. 17, 455 (2014).
- Kamitani, Y. & Tong, F. Decoding the visual and subjective contents of the human brain. Nat. Neurosci. 8, 679–685 (2005).
- Yan, Y. et al. Perceptual training continuously refines neuronal population codes in primary visual cortex. Nat. Neurosci. 17, 1380–1387 (2014).
- Morcos, A. S. & Harvey, C. D. History-dependent variability in population dynamics during evidence accumulation in cortex. *Nat. Neurosci.* 19, 1672–1681 (2016).
- Guyon, I., Weston, J., Barnhill, S. & Vapnik, V. Gene selection for cancer classification using support vector machines. *Mach. Learn.* 46, 389–422 (2002).

- Xu, H. et al. Acute in vivo testing of a conformal polymer microelectrode array for multi-region hippocampal recordings. J. Neural Eng. 15, 016017 (2018).
- Fiáth, R. et al. Long-term recording performance and biocompatibility of chronically implanted cylindrically-shaped, polymer-based neural interfaces. *Biomed. Eng./Biomedizinische Tech.* 63, 301–315 (2018).
- Yin, M. et al. Wireless neurosensor for full-spectrum electrophysiology recordings during free behavior. Neuron 84, 1170–1182 (2014).
- 33. Kim, C. et al. A 3 mm × 3 mm fully integrated wireless power receiver and neural interface system-on-chip. *IEEE Trans. Biomed. Circ. Syst.* **13**, 1736–1746 (2019).
- Zhou, A. et al. A wireless and artefact-free 128-channel neuromodulation device for closed-loop stimulation and recording in non-human primates. *Nat. Biomed. Eng.* 3, 15–26 (2019).
- 35. Cogan, S. F. Neural stimulation and recording electrodes. *Annu. Rev. Biomed. Eng.* **10**, 275–309 (2008).
- Kim, T.-i et al. Injectable, cellular-scale optoelectronics with applications for wireless optogenetics. Science 340, 211–216 (2013).
- Anikeeva, P. et al. Optetrode: a multichannel readout for optogenetic control in freely moving mice. Nat. Neurosci. 15, 163–170 (2012).
- Olafsdottir, H. F., Carpenter, F. & Barry, C. Task demands predict a dynamic switch in the content of awake hippocampal replay. *Neuron* 96, 925–935.e926 (2017).
- Wierzynski, C. M., Lubenov, E. V., Gu, M. & Siapas, A. G. State-dependent spike-timing relationships between hippocampal and prefrontal circuits during sleep. *Neuron* 61, 587–596 (2009).
- Euston, D. R., Tatsuno, M. & McNaughton, B. L. Fast-forward playback of recent memory sequences in prefrontal cortex during sleep. *Science* 318, 1147–1150 (2007).
- Wilber, A. A., Skelin, I., Wu, W. & McNaughton, B. L. Laminar organization of encoding and memory reactivation in the parietal cortex. *Neuron* 95, 1406–1419.e1405 (2017).
- Hahn, T. T., Sakmann, B. & Mehta, M. R. Differential responses of hippocampal subfields to cortical up-down states. *Proc. Natl Acad. Sci. USA* 104. 5169–5174 (2007).
- Tang, W., Shin, J. D., Frank, L. M. & Jadhav, S. P. Hippocampal-prefrontal reactivation during learning is stronger in awake compared with sleep states. J. Neurosci. 37, 11789–11805 (2017).
- Khodagholy, D., Gelinas, J. N. & Buzsáki, G. Learning-enhanced coupling between ripple oscillations in association cortices and hippocampus. *Science* 358, 369–372 (2017).
- 45. Gauthier, J. L. & Tank, D. W. A dedicated population for reward coding in the hippocampus. *Neuron* **99**, 179–193 (2018).
- Aronov, D., Nevers, R. & Tank, D. W. Mapping of a non-spatial dimension by the hippocampal-entorhinal circuit. *Nature* 543, 719–722 (2017).
- O'keefe, J. & Nadel, L. The Hippocampus as a Cognitive Map (Clarendon Press, 1978).
- 48. Eichenbaum, H., Kuperstein, M., Fagan, A. & Nagode, J. Cue-sampling and goal-approach correlates of hippocampal unit activity in rats performing an odor-discrimination task. *J. Neurosci.* 7, 716–732 (1987).
- 49. Trouche, S. et al. A hippocampus-accumbens tripartite neuronal motif guides appetitive memory in space. *Cell* 176, 1393–1406. e1316 (2019).

Publisher's note Springer Nature remains neutral with regard to jurisdictional claims in published maps and institutional affiliations.

© The Author(s), under exclusive licence to Springer Nature America, Inc. 2021

Methods

Array design and measurement. The Neuro-FITM array has 32 or 64 electrodes with a flexible shank (Fig. 1a,b and Extended Data Fig. 1). The electrodes are aligned in two rows that are 20 µm apart from either edge of the probe. The diameter of each electrode is 10 µm and the spacing between adjacent electrodes is 50 or 20 $\mu m.$ For the electrode designed to record in mouse hippocampus, the distance between the top and bottom electrodes is 750 µm, which is long enough to record from multiple depths of the CA1 region in the dorsal-ventral axis. The microelectrode array consists of a 1.55-mm probe and a 1.9-cm transparent flexible shank, connecting the electrodes to the ZIF connector. To determine the optimal length of the shank for shuttle-free insertion, we performed mechanical analysis as shown in equation (1), where $w = 170 \,\mu\text{m}$, $t = 16 \,\mu\text{m}$, L and $E = 3.2 \,\text{GPa}$ are the width, thickness, length and Young's modulus of the shank. The maximum force a probe can uphold without buckling is inversely proportional to the square of its length. As the insertion force F required to penetrate brain tissue was commonly accepted to be 1 mN50, we estimated that the length of the probe must be shorter than 1.9 mm. Therefore, we chose the length of the probe to be 1.8 mm, which was long enough to target the CA1 region of the mouse hippocampus, yet short enough to prevent buckling during insertion.

$$F_{\rm BF} = \frac{\pi^2 E w t^3}{5.88 L^2} \tag{1}$$

All electrochemical characterizations were performed with Gamry 600 Plus in 0.01 M phosphate-buffered saline (Sigma-Aldrich, catalog no. P3813 dry powder dissolved in deionized water). To measure the EIS and CV, we adopted a three-electrode configuration, where the Ag/AgCl (gauge 25) served as the reference electrode, and Pt (gauge 25) as the counter electrode. During EIS, the applied AC voltage was 20 mV, with frequency ranging from 100 kHz to 1 Hz at open circuit potential. We performed EIS of one representative array and the mean and s.d. are shown in Fig. 1k. During CV, the applied voltage between the PtNP/Au electrodes and the Ag/AgCl ones ranged from $-0.9\,\mathrm{V}$ to $1\,\mathrm{V}$ (Fig. 11). To stabilize the electrode/electrolyte interface, we performed CV of a representative channel. During the measurement of CV and EIS, we used a customized Faraday cage to shield from the 60-Hz powerline contamination and other electromagnetic noises.

Animals. All procedures were performed in accordance with protocols approved by the University of California San Diego (UCSD) Institutional Animal Care and Use Committee and guidelines of the National Institute of Health (NIH). Mice (cross between CaMKIIa-tTA:B6;CBA-Tg(Camk2a-tTA)1Mmay/J (JAX 003010) and tetO-GCaMP6s: B6;DBA-Tg(tetO-GCaMP6s)2Niell/J (JAX 024742), Jackson laboratories) were group housed in disposable plastic cages with standard bedding in a room with a reversed light cycle (12 h:12 h). Temperatures and humidity ranged from 18 °C to 23 °C and 40% to 60%, respectively. Experiments were performed during the dark period. Both male and female healthy adult mice (6 weeks or older) were used. Mice had no prior history of experimental procedures that could affect the results.

Surgery, multimodal experiments and data acquisition. Adult mice (6 weeks or older) were anesthetized with 1-2% isoflurane and injected with enrofloxacin (10 mg kg⁻¹) and buprenorphine (0.1 mg kg⁻¹) subcutaneously. A circular piece of scalp was removed to expose the skull. After cleaning the underlying bone using a surgical blade, a customized head-bar was implanted on to the exposed skull over the cerebellum (~1 mm posterior to lambda) with cyanoacrylate glue and cemented with dental acrylic (Lang Dental). Two stainless-steel wires (A-M Systems, catalog no. 791900) were implanted into the cerebellum as ground/ reference. The exposed skull was covered with cyanoacrylate glue applied several times. After cyanoacrylate glue formed a solid layer, a craniotomy (~0.5 mm in diameter, ~1.5-1.7 mm lateral and ~2.1-2.3 mm posterior to bregma) was made at the right hemisphere for microelectrode array insertion and the dura over the exposed brain surface was carefully removed. The microelectrode array was connected to the amplifier board first and held by a customized electrode holder attached to a micromanipulator (Sutter Instrument, catalog no. MP-285). The array was inserted at $\sim\!45\,\mu m\,s^{-1}$. Once inserted, the array was secured to the skull with Vetbond (3M). After the Vetbond became solid, the array was carefully released from the electrode holder and the exposed part of the array shank was bent to the right side of the animal. The amplifier board was fixed on to the right head-bar clamp arm on the stage (Fig. 2a and Extended Data Fig. 3a). Animals were fully awake before recordings. In six of eight animals, we successfully recorded SWRs and spikes in multiple recording channels. To quantify the accuracy of array implantation, we measured the distance between the target location and the actual location of the tip of the array based on the staining results (Extended Data Fig. 3b). We found that the distance was $100\pm33\,\mu\text{m}$ in the medial-lateral direction, $113\pm18\,\mu m$ in the anteroposterior direction and $87 \pm 24 \,\mu\text{m}$ in the vertical direction.

The wide-field calcium imaging was performed using a commercial fluorescence microscope (Axio Zoom.V16, Zeiss, objective lens (1×, 0.25 numerical aperture)) and a CMOS camera (ORCA-Flash4.0 v.2, Hamamatsu) through the intact skull as previously described 21 . Images were acquired using

HCImage Live (Hamamatsu) at 29.98 Hz, 512×512 pixels² (field of view, 11×11 mm²; binning, 4; 16 bit).

The microelectrode array was attached to a customized connector board that routed the electrical signals to the Intan RHD2132 amplifier boards (Intan Technologies). Electrophysiological recordings were performed using the Intan RHD 2000 system. The sampling rate was 30 kHz. For each animal, all recording sessions are on the same day with a 5- to 10-min interval between sessions. In total, six mice were recorded, each having two to three sessions. The length of each session was 1 h.

Immunohistochemistry. The microelectrode array was left in the brain for 4-5 weeks before perfusion to allow glial scar formation, which is a good indication of the array location. The mice were anesthetized (ketamine/xylazine, 150 mg kg⁻¹/12 mg kg⁻¹ of body weight) and perfused transcardially with 4% paraformaldehyde. Brains were then cryoprotected in a 30% sucrose solution overnight. Then, 50-mm coronal sections were cut with a microtome (Microm HM 430, Thermo Fisher Scientific) and blocked in a solution consisting of 4% normal donkey serum, 1% bovine serum albumin and 0.3% Triton X-100 in phosphate-buffered saline for 1 h at room temperature. They were then incubated overnight at 4°C with primary antibodies (1:1,000 chicken anti-green fluorescent protein (GFP), Aves Labs; 1:400 goat anti-glial fibrillary acidic protein (GFAP), Santa Cruz) diluted in the blocking solution. After washing, sections were then incubated in Alexa Fluor-conjugated secondary antibodies (1:1,000 anti-chicken 488; 1:1,000 anti-goat 594, Jackson Immuno Research) for 2h at room temperature. Slices were then mounted with a mounting medium for DAPI staining (Vector Laboratories) and imaged using a fluorescence microscope (ApoTome.2, Zeiss; Fig. 2b and Extended Data Fig. 3b).

SWR detection, spike sorting and $\Delta F/F$ processing. The detection of SWRs was performed using the following procedures. The raw LFP signals from the channels near CA1 pyramidal layers were bandpass filtered at $100-200\,\mathrm{Hz}$ (eighth-order Butterworth filter) in both forward and reverse directions to prevent phase distortion. Hilbert's transform was then used to obtain the envelope of the ripple-band signals. To detect the potential SWR events, we set a threshold to $2-3\,\mathrm{s.d.s}$ above the mean. Once the ripple-band envelope crossed the threshold, one candidate SWR event was labeled. The start and end times of this candidate SWR event were then defined as the times when the envelope just passed or returned back to the mean level. Between the start and end times, if the peak amplitude of the signal envelope further exceeded $4-6\,\mathrm{s.d.s}$ above the mean, then an SWR event was finally identified. Note that, similar to other studies 51,52 , we considered only SWR events with a duration $>20\,\mathrm{ms.}$

The spike sorting was performed with Kilosort 2 (ref. ⁵³) and the output results were followed by manual curation. The recording sessions from the same day were pooled before the spike sorting to identify the same neurons across sessions. The LFP data were first high-pass filtered at 250 Hz (third-order Butterworth filter) and whitened to remove the correlation between nearby channels. Then the Kilosort algorithm identified the best templates and the putative clusters of neurons, along with their spike timing and amplitudes. These preliminary results were further manually refined by merging the same neurons, splitting different neurons and labeling low-amplitude inseparable spikes as multi-unit activities. Finally, the hippocampus pyramidal cells and interneurons were classified based on the firing rates and the asymmetry of the spike waveforms ⁵⁴.

To obtain the $\Delta F/F$ time series from the wide-field calcium imaging data, images of 512 × 512 pixels2 were first down-sampled to 128 × 128 pixels2. For each pixel, time-varying baseline fluorescence (F) was estimated for a given time point as the 10th percentile value >180 s around it. For the start and end of each imaging block, the following and preceding 90-s windows were used to determine the baseline, respectively. The raw $\Delta F/F$ of each pixel was z-score normalized. We corrected for hemodynamic contamination following published procedures21. Briefly, we performed principal component analysis (PCA) followed by independent component analysis (ICA)²¹ on z-score-normalized $\Delta F/F$ to extract hemodynamic components from the total signal. We first performed PCA and preserved the top 50 PCs, which explained ~95% variance of the data. Then the spatial ICA was performed over the top 50 PCs to generate 50 spatially independent modules. Finally, the modules containing the vasculature activities were excluded and the reconstruction of cortical activity was done with the remaining modules. We screened different numbers of components (20, 40, 50, 150 and 200) preserved in PCA/ICA analysis and, using 50 components, gave the best separation of hemodynamic and neural signal. To obtain the $\Delta F/F$ of each cortical region, the dorsal cortex was manually parcellated into individual regions based on the Allen Brain Atlas (Fig. 5b) and the $\Delta F/F$ time series was computed as the mean of the pixel values within each cortical region.

The time delay between cortical activation and SWRs. For the analysis of the timing of SWR onset and the onset of dorsal cortex activity averaged across SWR events (Fig. 5a and Extended Data Fig. 4), we included only the well-separated SWRs that did not have any preceding SWR events for at least 3 s. This was to prevent potential contamination from the tail of cortical activity associated with preceding SWRs. The onset timing of the event-averaged cortical activity was

defined as the earliest activity onset across 16 cortical regions. For each region, using the $\Delta F/F$ at $-2\,\mathrm{s}$ relative to SWR onset as the baseline, we performed rank-sum tests at each frame between $-2\,\mathrm{s}$ and 2 s relative to SWR onset. The activity onset time for each cortical region was defined as the time when its $\Delta F/F$ was significantly higher (P < 0.05) than the baseline for at least three consecutive frames. The mean onset time was computed by first averaging across sessions within animals and later averaging across animals. The peak time of event-averaged cortical activity was defined as the time when cortical activity averaged across 16 regions reached the maximum value. The mean peak time was computed by first averaging across sessions within animals and then averaging across animals.

For the analysis of timing between SWR onset and the activity onset of each cortical region during individual SWRs (Fig. 5d,e and Extended Data Fig. 5), we also focused on well-separated SWR events. The activity onset of each cortical region was identified as previously described21. In brief, we first computed the derivative of the smoothed $\Delta F/F$ traces (loess, 1-s window) and defined the inactive segments as the periods with the derivative within 1 s.d. of the whole derivative trace. Then we defined $\Delta F/F$ events as the periods when the derivative exceeded the 1 s.d. of the inactive period. For each event, the onset time was first estimated as the time when the derivative exceeded the 1 s.d. criterion, and the offset time was estimated as the time when the derivative dropped to <0 for the first time after the onset. To further refine the onset time, for each event, the baseline $\Delta F/F$ was defined as the value at the first time point when the derivative was >0 before the offset time, and $\Delta F/F$ noise level was defined as the mean of the absolute difference between the raw and smoothed $\Delta F/F$ traces. The onset was further refined as the last time point before the offset time when the $\Delta F/F$ value is within the noise level from the baseline $\Delta F/F$.

After identifying the activity onset of each cortical region, we determined the timing of each SWR onset relative to the activity onset of each region using the following procedures. For each SWR onset, we first examined the slope of the instantaneous $\Delta F/F$ traces of one region. If the $\Delta F/F$ was rising, we looped backward in time frame by frame until reaching -1 s before the SWR onset. If a cortical activity onset was detected within this time interval, we labeled this SWR event as occurring after the cortical activity onset. On the other hand, if the $\Delta F/F$ was not rising, we looped forward in time frame by frame until reaching +1 s after the SWR onset. If a cortical activity onset was detected within this time interval, we labeled this SWR event as occurring before the cortical activity onset. The above procedure was done for every well-separated SWR and all the cortical regions.

Two-stage TCA algorithm. To prepare the data for the TCA algorithm, we performed the preprocessing procedures described below. The $\Delta F/F$ traces in each cortical region were z-score normalized within each recording session. For each SWR event, we used the 3-s $\Delta F/F$ traces (1 s before SWR onset, 2 s after) from 16 cortical regions to construct a 2D data matrix (region×time). Then we concatenated the 2D data matrices from all the SWR events to form a three-dimensional (3D) data tensor (region×time×event). Finally, the data tensors from all the six mice were concatenated along the event dimension to form a big data tensor (Fig. 6a).

The TCA has been demonstrated to be effective in discovering the low-dimensional dynamics of neural activity¹³. However, as the original algorithm did not guarantee achieving the global optimum, the results could vary from run to run. To achieve reliable results, we devised a two-stage TCA algorithm, which includes a pre-clustering step to alleviate the variations from individual runs. The detailed procedure is shown in Extended Data Fig. 6a. The first stage of the algorithm consisted of fitting a TCA model with a sufficiently high rank order. The tensor toolbox v.3.0 (https://www.tensortoolbox.org) was used to perform TCA decomposition. To determine this rank order, we fitted multiple TCA models with rank 2-15 and examined the reconstruction error of each TCA model. The reconstruction error started to show diminishing returns toward rank 15 (Extended Data Fig. 6b). Therefore, we chose rank 15 for the initial TCA and ran it 100 times. Each result gave a slightly different decomposition of the original high-dimensional data. To capture the underlying dynamics that were common and consistent in most TCA results, we performed clustering of the 1,500 TCA spatiotemporal patterns by computing the similarity matrix using 2D correlation. Then the community detection algorithm was performed with the community detection toolbox (http://netwiki.amath.unc.edu/GenLouvain/GenLouvain) to identify the clusters. As shown in the sorted similarity matrix (Extended Data Fig. 6c), we identified eight different clusters of TCA patterns. The number of patterns assigned to each cluster is shown in Extended Data Fig. 6d. Examples of randomly chosen patterns assigned to each cluster are shown in Extended Data Fig. 6f. The second stage of the TCA algorithm used the centroids of eight clusters identified from the first stage to initialize the region and time factors, leaving all the event factors randomly initialized. Then we ran the TCA optimization algorithm as before until it converged to obtain the final set of TCA factors (Extended Data Fig. 7a). Compared with the original TCA algorithm, our two-stage TCA algorithm gave significantly lower reconstruction error $(P=1.38\times10^{-11}; Extended Data Fig. 6e).$

Cortical pattern assignment. To assign the cortical activity pattern of each SWR event to one of the eight spatiotemporal templates (Fig. 6b), we computed the 2D

correlation between the *z*-score-normalized $\Delta F/F$ traces and each template. If the correlation value for one pattern was higher than a threshold (0.45; Fig. 6c–e), we assigned the SWR event to that pattern. If one SWR event was assigned to multiple patterns, we excluded that SWR event.

The algorithm for pairwise discrimination of the cortical patterns. To discriminate the cortical patterns based on hippocampal activity, we used the SVM. The hippocampal neuron firing counts during 0-100 ms relative to SWR onset were used as input features for the SVM algorithm. As the numbers of SWR events assigned to each cortical pattern template were often unbalanced (Fig. 6e), we modified the misclassification costs to be inversely proportional to the sample frequencies of the two pattern types in each pair, N1 and N2. Therefore, misclassifying pattern type 1 as pattern type 2 had cost N2/(N1+N2), whereas misclassifying pattern type 2 as pattern type 1 had cost N1/(N1 + N2). Also, to measure the decoding performance, we used balanced accuracy instead of the accuracy, which could be misleading in the unbalanced datasets. The balanced accuracy was defined as the average of the correct proportion for each class (that is, cortical pattern). We performed the recursive feature elimination 29,55 to identify the discriminant neurons for each cortical pattern pair (Extended Data Fig. 9). This was done by choosing the subset of neurons that give the highest balanced accuracy in the leave-one-out cross-validation. To evaluate whether the decoding performance for each cortical pattern pair was significantly better than chance, we randomly shuffled the cortical pattern identities 2,000 times, performed SVM using the identified discriminant neurons and computed the balanced accuracy in each shuffle to obtain a null distribution of it. Then we computed the P value based on the balanced accuracy from the original dataset and the distribution of the balanced accuracy from the shuffled dataset (Fig. 7c, and Extended Data Figs. 10b and 8). The exact \dot{P} values associated with Fig. 7c are as follows: mouse 1: P(1-2) = 0.086, P(1-3) = 0.2815, P(1-4) = 0.1415, P(1-5) = 0.153, P(1-6) = 0.0035, P(1-7) = 0.094, P(1-8) = 0.0965, P(2-3) = 0.3365, P(2-4) = 0.0315, P(2-5) = 0.036, P(2-6) = 0.0535, P(2-7) = 0.0245, P(2-8) = 0.0425, P(3-4) = 0.5235, P(3-5) = 0.28, P(3-6) = 0.052, P(3-7) = 0.037, P(3-8) = 0.3795, P(4-5) = 0.13, P(4-6) = 0.0695,P(4-7) = 0.005, P(4-8) = 0.016, P(5-6) = 0.153, P(5-7) = 0.017, P(5-8) = 0.062, P(6-7) = 0.0205, P(6-8) = 0.0025, P(7-8) = 0.0275; mouse 2: P(1-2) = 0.0035, P(1-3)=0.0045, P(1-4)=0.004, P(1-5)=0.0665, P(1-6)=0, P(1-7)=0, P(1-8)=0, P(2-3) = 0.009, P(2-4) = 0.017, P(2-5) = 0.0525, P(2-6) = 0.0375, P(2-7) = 0.0055, P(2-8) = 0.0005, P(3-4) = 0.039, P(3-5) = 0.007, P(3-6) = 0.0545, P(3-7) = 0.035, P(3-8) = 0.0025, P(4-5) = 0.0125, P(4-6) = 0.001, P(4-7) = 0.002, P(4-8) = 0, P(5-6) = 0.0085, P(5-7) = 0.006, P(5-8) = 0.0015, P(6-7) = 0, P(6-8) = 0.001,P(7-8) = 0; mouse 3: P(1-2) = 0.0105, P(1-3) = 0.015, P(1-4) = 0.024, P(1-5) = 0.0275, P(1-6) = 0.0035, P(1-7) = 0, P(1-8) = 0.0295, P(2-3) = 0.008, P(2-4) = 0.006, P(2-5) = 0.017, P(2-6) = 0.2245, P(2-7) = 0.0015, P(2-8) = 0.0135,P(3-4) = 0.0005, P(3-5) = 0.017, P(3-6) = 0.1865, P(3-7) = 0.001, P(3-8) = 0.015,P(4-5) = 0.047, P(4-6) = 0.001, P(4-7) = 0.0035, P(4-8) = 0.041, P(5-6) = 0.0035, P(5-7) = 0, P(5-8) = 0.0165, P(6-7) = 0.0295, P(6-8) = 0.034, P(7-8) = 0.2295; mouse 4: P(1-2) = 0.0055, P(1-3) = 0.0085, P(1-4) = 0.023, P(1-5) = 0.0135, P(1-6) = 0.054, P(1-7) = 0.0135, P(1-8) = 0.167, P(2-3) = 0.073, P(2-4) = 0.013, P(2-5) = 0.037, P(2-6) = 0.0765, P(2-7) = 0.3305, P(2-8) = 0.1825, P(3-4) = 0.25, P(3-5) = 0.0675, P(3-6) = 0.0175, P(3-7) = 0.03, P(3-8) = 0.029, P(4-5) = 0.034, P(4-6) = 0.0905, P(4-7) = 0.0375, P(4-8) = 0.0675, P(5-6) = 0.0015, P(5-7) = 0.0775, P(5-8) = 0.0285, P(6-7) = 0.046, P(6-8) = 0.094, P(7-8) = 0.39; mouse 5: P(1-2) = 0.0335, P(1-3) = 0.0755, P(1-4) = 0.009, P(1-5) = 0.0075, P(1-6) = 0.013, P(1-7) = 0, P(1-8) = 0.0055, P(2-3) = 0.0295, P(2-4) = 0.0145, P(2-5) = 0.0495, P(2-6) = 0.057, P(2-7) = 0.0215, P(2-8) = 0.1255, P(3-4) = 0.0875, P(3-5) = 0.0195, P(3-6) = 0.015, P(3-7) = 0.0095, P(3-8) = 0.0535, P(4-5) = 0.0155, P(4-6) = 0.009, P(4-7) = 0.0325, P(4-8) = 0.0245, P(5-6) = 0.0145, P(5-7) = 0.0415, P(5-8) = 0.026, P(6-7) = 0.007, P(6-8) = 0.0065, P(7-8) = 0.1315; mouse 6: P(1-2) = 0.018, P(1-3) = 0.0175, P(1-4) = 0.017, P(1-5) = 0.0065, P(1-6) = 0.046, P(1-7) = 0.013, P(1-8) = 0.001, P(2-3) = 0.007, P(2-4) = 0.0105, P(2-5) = 0.108, P(2-6) = 0.0115, P(2-7) = 0.1615, P(2-8) = 0.0025, P(3-4) = 0.0345, P(3-5)=0.0025, P(3-6)=0.008, P(3-7)=0.001, P(3-8)=0.0045, P(4-5)=0.0835,P(4-6) = 0.0015, P(4-7) = 0.062, P(4-8) = 0.017, P(5-6) = 0.0315, P(5-7) = 0.03, P(5-8) = 0.0065, P(6-7) = 0.0055, P(6-8) = 0.0025, P(7-8) = 0.0125. The exact P values associated with Extended Data Fig. 10b are as follows: mouse 1: P(1-2) = 0.0645, P(1-3) = 0.1735, P(1-4) = 0.0315, P(1-5) = 0.057, P(1-6) = 0.128, P(1-7) = 0.008, P(1-8) = 0.027, P(2-3) = 0.1735, P(2-4) = 0.0375, P(2-5) = 0.0025, P(2-6) = 0.0205, P(2-7) = 0.0135, P(2-8) = 0.345, P(3-4) = 0.1685, P(3-5) = 0.0225, P(3-6) = 0.012, P(3-7) = 0.04, P(3-8) = 0.3775, P(4-5) = 0.01, P(4-6) = 0.3415, P(4-7) = 0.0415, P(4-8) = 0.289, P(5-6) = 0.042, P(5-7) = 0.1595, P(5-8) = 0.066, P(6-7) = 0.473, P(6-8) = 0.01, P(7-8) = 0.07; mouse 2: P(1-2) = 0.018, P(1-3)=0.034, P(1-4)=0.007, P(1-5)=0.114, P(1-6)=0.0065, P(1-7)=0.0245, P(1-8) = 0, P(2-3) = 0.0135, P(2-4) = 0.012, P(2-5) = 0.0115, P(2-6) = 0.037, P(2-7) = 0.0205, P(2-8) = 0, P(3-4) = 0.058, P(3-5) = 0, P(3-6) = 0.02, P(3-7) = 0.0345, P(3-8) = 0.0035, P(4-5) = 0.0115, P(4-6) = 0.0015, P(4-7) = 0, P(4-8) = 0, P(5-6) = 0.0465, P(5-7) = 0.009, P(5-8) = 0, P(6-7) = 0, P(6-8) = 0, P(7-8) = 0; mouse 3: P(1-2) = 0, P(1-3) = 0.001, P(1-4) = 0.0135, P(1-5) = 0.035, P(1-6) = 0.011, P(1-7) = 0.0935, P(1-8) = 0.001, P(2-3) = 0.0575, P(2-4) = 0.0015, P(2-5) = 0.003, P(2-6) = 0.0515, P(2-7) = 0.0045, P(2-8) = 0.0015, P(3-4) = 0.0015

=0.0025, P(3-5)=0.0225, P(3-6)=0.2895, P(3-7)=0.0045, P(3-8)=0.0025,

P(4-5) = 0.002, P(4-6) = 0.0295, P(4-7) = 0.002, P(4-8) = 0.0205, P(5-6) = 0.023, P(5-7) = 0.0055, P(5-8) = 0.01, P(6-7) = 0.088, P(6-8) = 0.002, P(7-8) = 0.0355; mouse 4: P(1-2) = 0.221, P(1-3) = 0.177, P(1-4) = 0.111, P(1-5) = 0.0335, P(1-6) = 0.011, P(1-7) = 0.0175, P(1-8) = 0.0435, P(2-3) = 0.0765, P(2-4) = 0.0025, P(2-5) = 0.0205, P(2-6) = 0.0615, P(2-7) = 0.001, P(2-8) = 0.143, P(3-4) = 0.2925, P(3-5) = 0.0335, P(3-6) = 0.009, P(3-7) = 0.049, P(3-8) = 0.0335, P(4-5) = 0.0105, P(4-6) = 0.123, P(4-7) = 0.022, P(4-8) = 0.1275, P(5-6) = 0.0195, P(5-7) = 0.105, P(5-8) = 0.1305, P(6-7) = 0.0875, P(6-8) = 0.0255, P(7-8) = 0.11; mouse 5: P(1-2) = 0.085, P(1-3) = 0.627, P(1-4) = 0.1625, P(1-5) = 0.4755, P(1-6) = 0.024, P(1-7) = 0.259, P(1-8) = 0.009, P(2-3) = 0.105, P(2-4) = 0.052, P(2-5) = 0.1565, P(2-6) = 0, P(2-7) = 0.0065, P(2-8) = 0.09, P(3-4) = 0.142, P(3-5) = 0.0705, P(3-6) = 0.176, P(3-7) = 0.014, P(3-8) = 0.12, P(4-5) = 0.0705, P(4-6) = 0.0015, P(4-7) = 0.2375, P(4-8) = 0.007, P(5-6) = 0.001, P(5-7) = 0.185, P(5-8) = 0.0995, P(6-7) = 0.0075, P(6-8) = 0.0105, P(7-8) = 0.115; mouse 6: P(1-2) = 0.063, P(1-3) = 0.021, P(1-4) = 0.023, P(1-5) = 0.0065, P(1-6) = 0.0995, P(1-7) = 0.013, P(1-8) = 0.1085, P(2-3) = 0.01, P(2-4) = 0.0105, P(2-5) = 0.004, P(2-6) = 0.0455, P(2-7) = 0.0925, P(2-8) = 0.0005, P(3-4) = 0.008, P(3-5) = 0.004, P(3-6) = 0.044, P(3-7) = 0.003, P(3-8) = 0.0165, P(4-5) = 0.0105, P(4-6) = 0.034, P(4-7) = 0.2415, P(4-8) = 0.077, P(5-6) = 0.011, P(5-7) = 0.0035, P(5-8) = 0.045, P(6-7) = 0.0035,P(6-8) = 0.033, P(7-8) = 0.012. Finally, to further quantify the overall decoding performance for each mouse, we computed the fraction of distinguishable cortical pattern pairs (P<0.05) over the cortical pattern pairs included in the analysis within each animal (Fig. 7d and Extended Data Fig. 10c). To examine whether the fraction of distinguishable cortical pattern pairs in each animal is significant, we tested against the null hypothesis that the fraction is obtained by chance. As the probability of each pattern pair being mislabeled as distinguishable is 0.05, under the null hypothesis, the number of distinguishable pairs in each mouse follows a binomial distribution where the parameter P = 0.05 and N equals the number of pattern pairs included in the analysis within each animal. Therefore, the critical number of pattern pairs, Nc, is determined as the smallest integer that makes the binomial cumulative density function >0.95. Finally, the chance level fraction is obtained as the ratio between Nc and N.

Hippocampal neuron firing rates under different cortical patterns during

SWRs. To obtain the instantaneous firing rates between $-1\,\mathrm{s}$ and $2\,\mathrm{s}$ relative to SWR onset for each hippocampal neuron, we used 100-ms time bins without overlap for each SWR event (Fig. 7a and Extended Data Fig. 10a). We defined the preference index (PI) to measure whether one neuron showed higher activity for one pattern than the other (Fig. 7e and Extended Data Fig. 10d). For each pattern pair (for example, pattern X and pattern Y), the preference index of one neuron was calculated using its mean firing count between 0 and 100 ms relative to SWR onset under each pattern, as shown in equation (2).

$$PI(X) = \frac{Firing count (X) - Firing count (Y)}{Firing count (X) + Firing count (Y)}$$
(2)

The early versus the late group included pattern pairs of pattern 1 versus 2, 1 versus 3, 2 versus 3, 4 versus 5, 4 versus 6 and 5 versus 6. The anterior versus posterior group included pattern pairs of pattern 1 versus 4, 2 versus 5 and 3 versus 6. For each cortical pattern pair, the preference index at population level was calculated by averaging across discriminant hippocampal neurons (Fig. 7e and Extended Data Fig. 10d).

Statistics and reproducibility. For electrode arrays designed for recordings in mice, rats and monkeys, four electrode arrays were imaged, respectively, and example images are shown in Fig. 1 and Extended Data Fig. 1. Two animals were excluded from eight animals from recordings and analyses due to unsuccessful implantations. The six animals with successful implantations went through the same recording procedures and were all included in analyses. All statistical analyses were performed in MATLAB. Statistical tests were two tailed and significance was defined by an α pre-set to 0.05. Error bars and shaded regions surrounding line plots indicate ±s.e.m. unless otherwise noted. All the statistical tests are described in the figure legends and each test was selected based on data distributions using histograms. For Fig. 1m, a two-sided Student's t-test was used to test the correlation between the electrode impedance and the recording noise level. For Fig. 5d,e, a two-tailed bootstrap test (10,000×) was used to test the median time difference between SWR and cortical activity onset and the fraction of SWR events occurring before or after cortical activity onset. For Fig. 7c, the decodable pattern pair was determined by a one-tailed shuffling test, which randomly permuted the labels of cortical patterns. For Fig. 7d, the chance level number of decodable pattern pairs (nc) was computed from the inverse of binomial cumulative distribution with probability 0.95 and the chance level fraction was obtained by dividing nc with n=28, the number of pattern pairs on which decoding was performed. For Fig. 7e, a two-tailed bootstrap test (10,000×) was used to determine the significance of preference index and the balanced accuracy. Multiple comparisons were corrected for using Benjamini–Hochberg corrections. Sample sizes (n) are as follows where applicable: recording sessions per animal, 2, 3, 3, 3, 2, 2; well-separated SWRs/ all SWRs per animal, 530/1,245, 896/1,785, 787/1,440, 826/1,618, 673/1,365, 578/1,190; hippocampal neurons per animal, 8, 21, 14, 11, 10, 10. No statistical

methods were used to predetermine sample size but our sample sizes are similar to those reported in previous publications from our lab³¹ and others using wide-field calcium imaging^{56,57} and electrophysiological recordings⁵⁸. No randomization was performed. Randomization is not necessary to our study because all animals underwent the same surgical and recording procedures. Data collection and analysis were not performed blind to the conditions of the experiments.

Reporting Summary. Further information on research design is available in the Nature Research Reporting Summary linked to this article.

Data availability

Data are available upon request from the authors. The Allen Brain Atlas could be accessed through Brain Explorer 2: http://mouse.brain-map.org/static/brainexplorer. Source data are provided with this paper.

Code availability

The codes for ripple detection, two-stage TCA and the pairwise decoding of cortical patterns are available at https://github.com/xinliuucsd/hippocampus-cortex.

References

- Weltman, A., Yoo, J. & Meng, E. Flexible, penetrating brain probes enabled by advances in polymer microfabrication. *Micromachines* 7, 180 (2016).
- Patel, J., Schomburg, E. W., Berényi, A., Fujisawa, S. & Buzsáki, G. Local generation and propagation of ripples along the septotemporal axis of the hippocampus. J. Neurosci. 33, 17029–17041 (2013).
- Roux, L., Hu, B., Eichler, R., Stark, E. & Buzsáki, G. Sharp wave ripples during learning stabilize the hippocampal spatial map. *Nat. Neurosci.* 20, 845–853 (2017).
- Pachitariu, M., Steinmetz, N. A., Kadir, S. N., Carandini, M. & Harris, K. D.
 Fast and accurate spike sorting of high-channel count probes with KiloSort.
 Adv. Neural Inf. Process. Syst. 29, 4448–4456 (2016).
- Zutshi, I. et al. Recurrent circuits within medial entorhinal cortex superficial layers support grid cell firing. *Nat. Commun.* 9, 3701 (2018).
- Diamantaki, M. et al. Manipulating hippocampal place cell activity by single-cell stimulation in freely moving mice. Cell Rep. 23, 32–38 (2018).
- Musall, S., Kaufman, M. T., Juavinett, A. L., Gluf, S. & Churchland, A. K. Single-trial neural dynamics are dominated by richly varied movements. *Nat. Neurosci.* 22, 1677–1686 (2019).
- Pinto, L. et al. Task-dependent changes in the large-scale dynamics and necessity of cortical regions. *Neuron* 104, 810–824.e819 (2019).
- Clancy, K. B., Orsolic, I. & Mrsic-Flogel, T. D. Locomotion-dependent remapping of distributed cortical networks. *Nat. Neurosci.* 22, 778–786 (2019).

Acknowledgements

We thank Q. Chen, O. Arroyo and L. Hall for technical assistance, and members of the Kuzum and Komiyama labs for discussions. This research was supported by grants from the Office of Naval Research (grants N000142012405 and N00014162531), the National Science Foundation (NSF; grants ECCS-2024776, ECCS-1752241 and ECCS-1734940) and the NIH (grants R21 EY029466, R21 EB026180 and DP2 EB030992) to D.K., and grants from the NIH (grants R01 NS091010A, R01 EY025349, R01 DC014690, R21 NS109722 and P30 EY022589), Pew Charitable Trusts and David & Lucile Packard Foundation to T.K. Fabrication of the electrodes was performed at the San Diego Nanotechnology Infrastructure of UCSD, a member of the National Nanotechnology Coordinated Infrastructure, which is supported by the NSF (grant ECCS-1542148).

Author contributions

This work was conceived by D.K. and T.K. Y. Lu and J.H.K. performed microelectrode array fabrication and characterization. C.R. and X.L. performed all animal experiments. X.L. and C.R. analyzed them, with contributions from Y.L., S.L., T.K. and D.K. X.L., C.R., D.K. and T.K. wrote the manuscript and all the authors edited it.

Competing interests

The authors declare no competing interests.

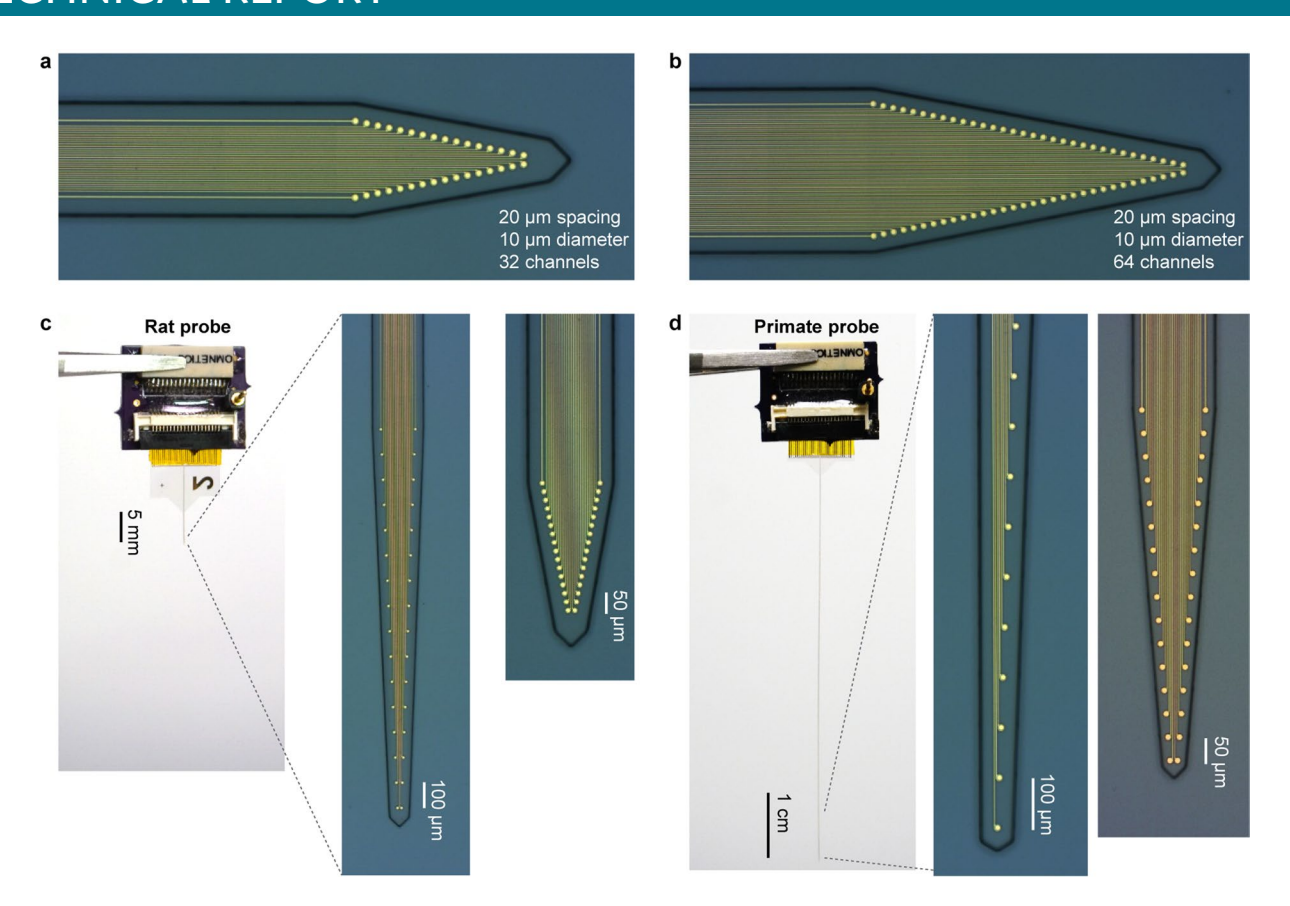
Additional information

Extended data is available for this paper at https://doi.org/10.1038/s41593-021-00841-5.

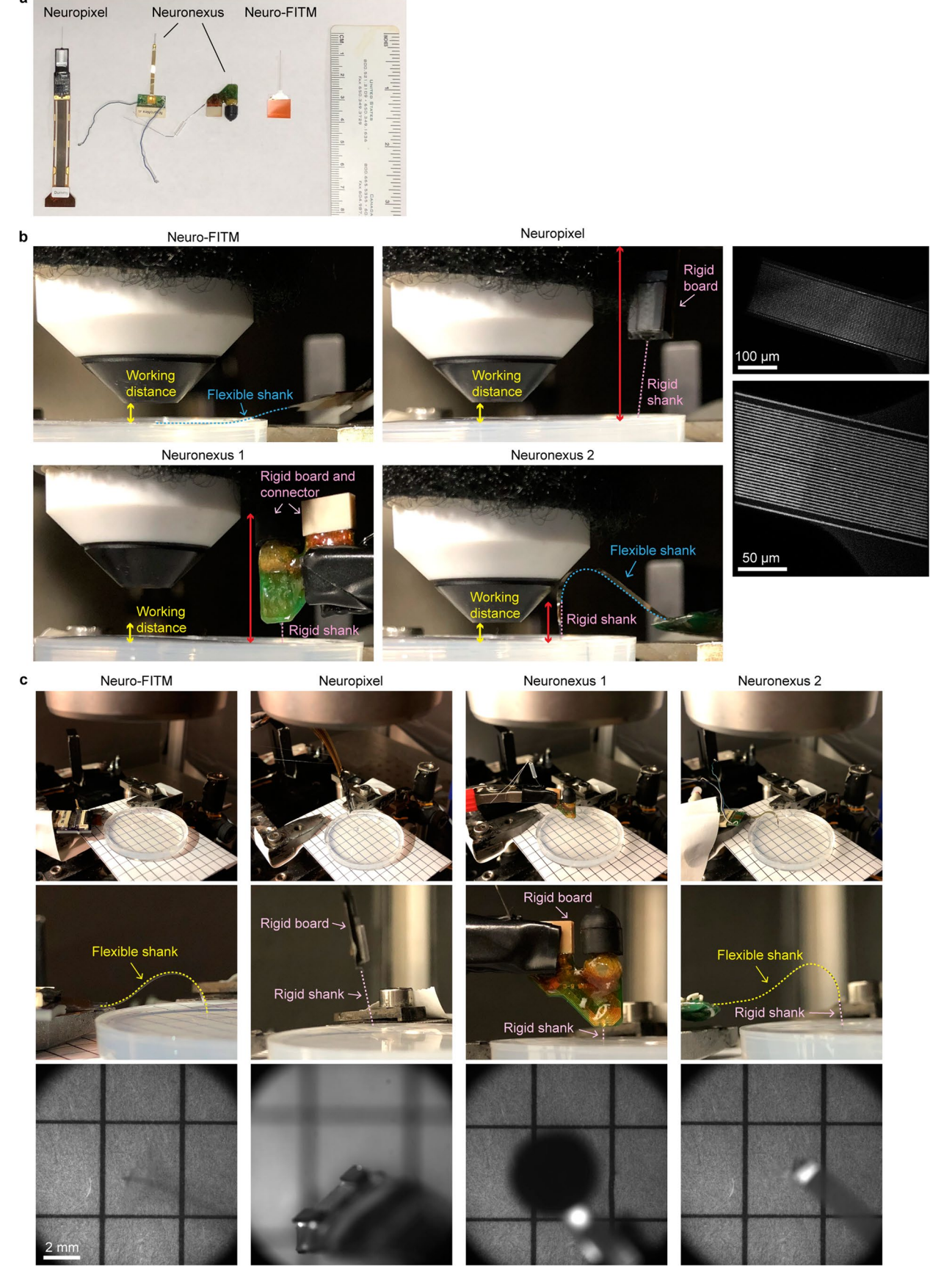
 $\label{thm:contains} \textbf{Supplementary information} \ The online version contains supplementary material available at $$https://doi.org/10.1038/s41593-021-00841-5.$

Correspondence and requests for materials should be addressed to T.K. or D.K.

Peer review information *Nature Neuroscience* thanks Benjamin Scott and the other, anonymous, reviewer(s) for their contribution to the peer review of this work.**Reprints** and permissions information is available at www.nature.com/reprints.



Extended Data Fig. 1 | Microscope pictures of different Neuro-FITM probe designs. a, Microscope image of the recording tip of 32 channel Neuro-FITM array with 20 μ m spacing. **b**, Same as (a), but for 64 channel Neuro-FITM array with 20 μ m spacing. **c**, Picture of the whole probe (left), the microscope pictures of the recording tip of 32 channel Neuro-FITM array with 100 μ m spacing (middle) and 20 μ m spacing (right) for recording in rats. **d**, Same as **c**, but for 32 channel Neuro-FITM array with 100 μ m spacing for recording in primates.

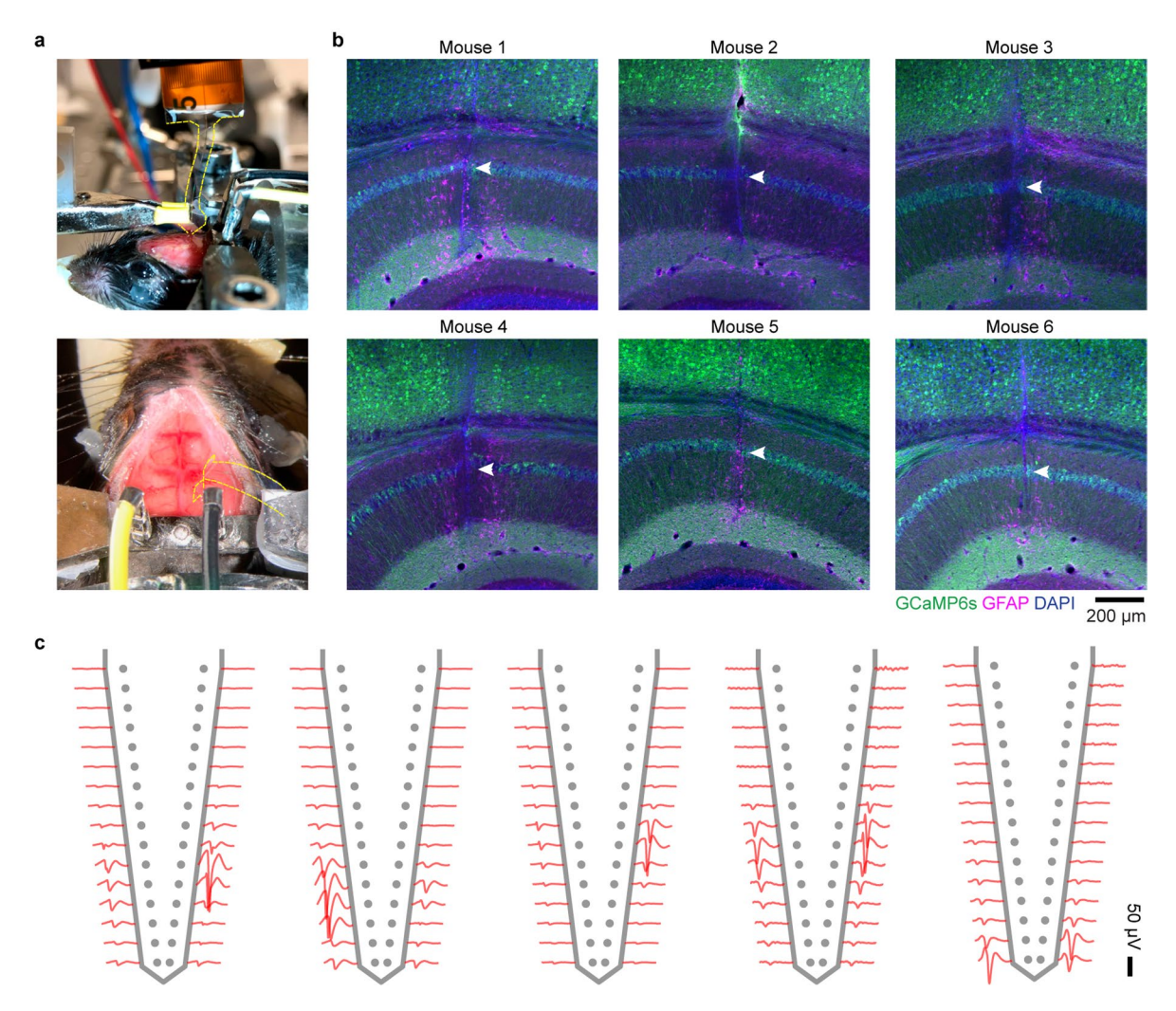


Extended Data Fig. 2 | See next page for caption.

TECHNICAL REPORT

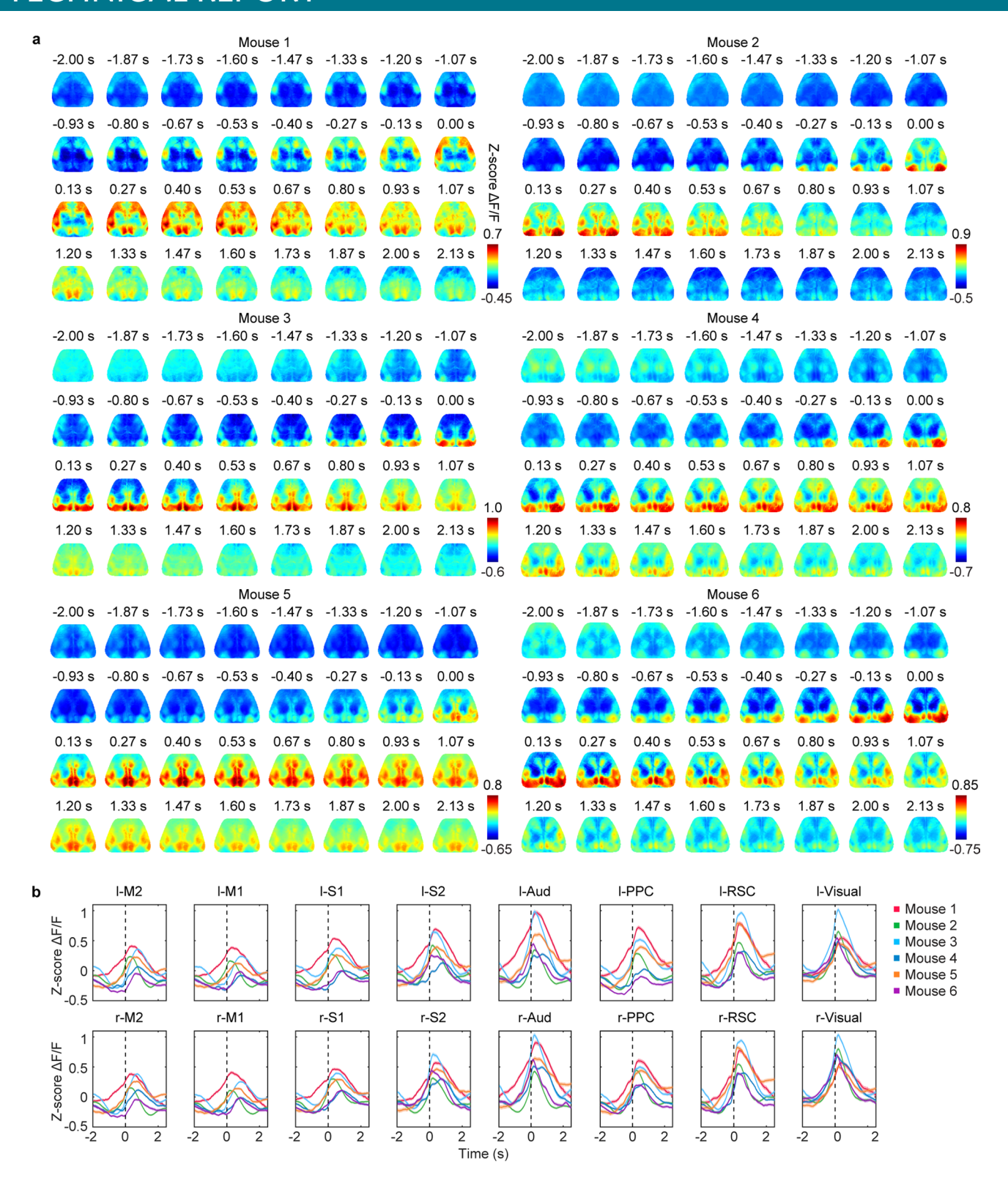
NATURE NEUROSCIENCE

Extended Data Fig. 2 | Testing the multimodal recording setup using Neuro-FITM and standard silicon probes under both the wide-field and 2-photon imaging systems. a, A picture of the probes tested in the multimodal recording setup. **b**, Pictures of the side view under the 2-photon imaging system. Neuro-FITM can be completely bent to the side as shown with the blue dashed line. Both the Neuronexus probes and the Neuropixel probe prevent the lowering of microscope objective (total rigid part indicated by red double arrow). The right column are the 2-photon images of the array surface, showing the thin Au wires, the boundary of the array substrate, and the penetration point. **c**, Pictures of the experimental setup (top), the zoom-in side view (middle), and the field of view (bottom) under wide-field imaging system, showing the blocking of field of view (Neuronexus probes) and preventing the lowering of microscope objective (Neuropixel probe). Wide-field image shows that mostly transparent Neuro-FITM does not block the field of view or generate shadows.

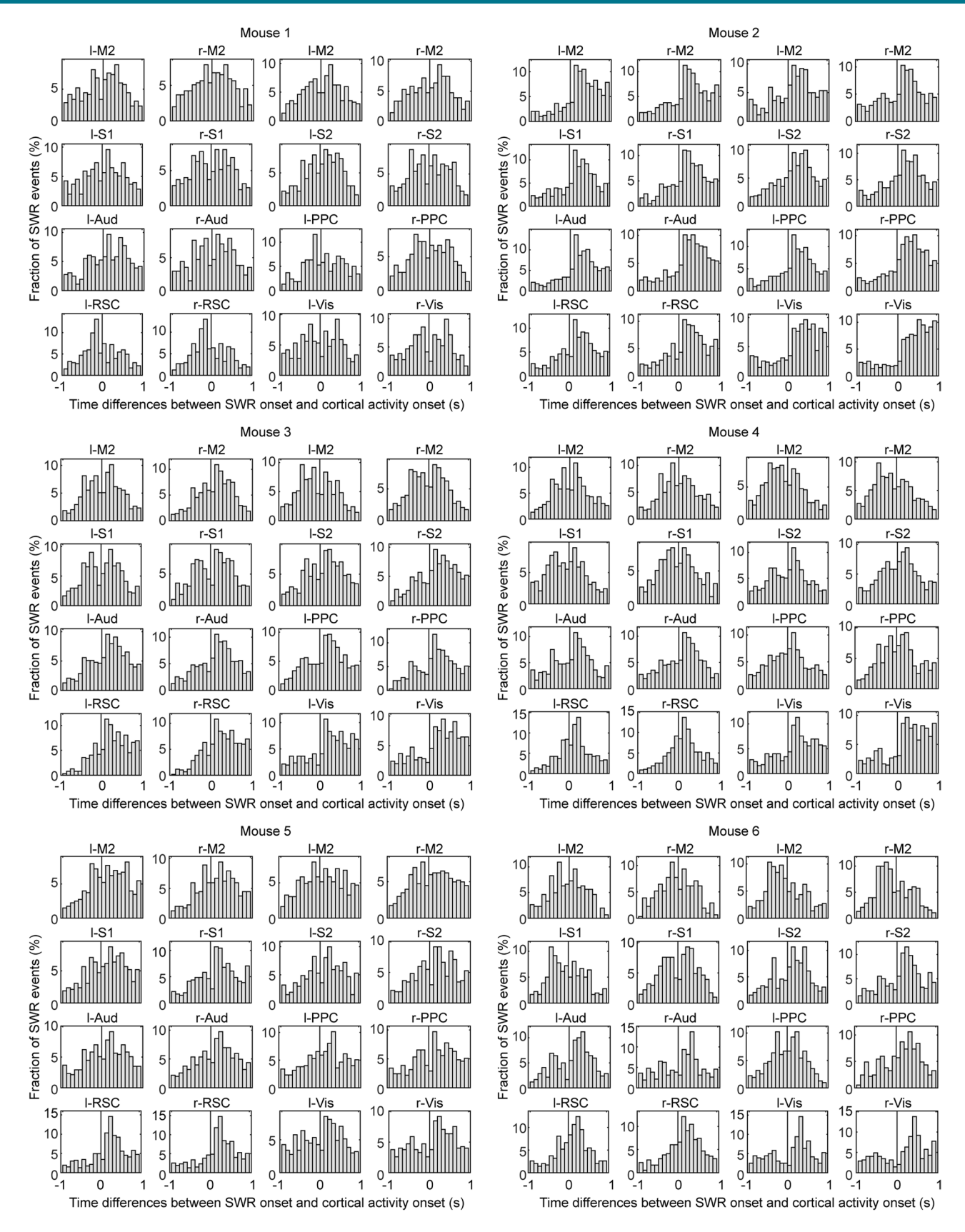


Extended Data Fig. 3 | Implantation of Neuro-FITM array to hippocampus in in vivo experiments and the spike waveforms of example neurons.

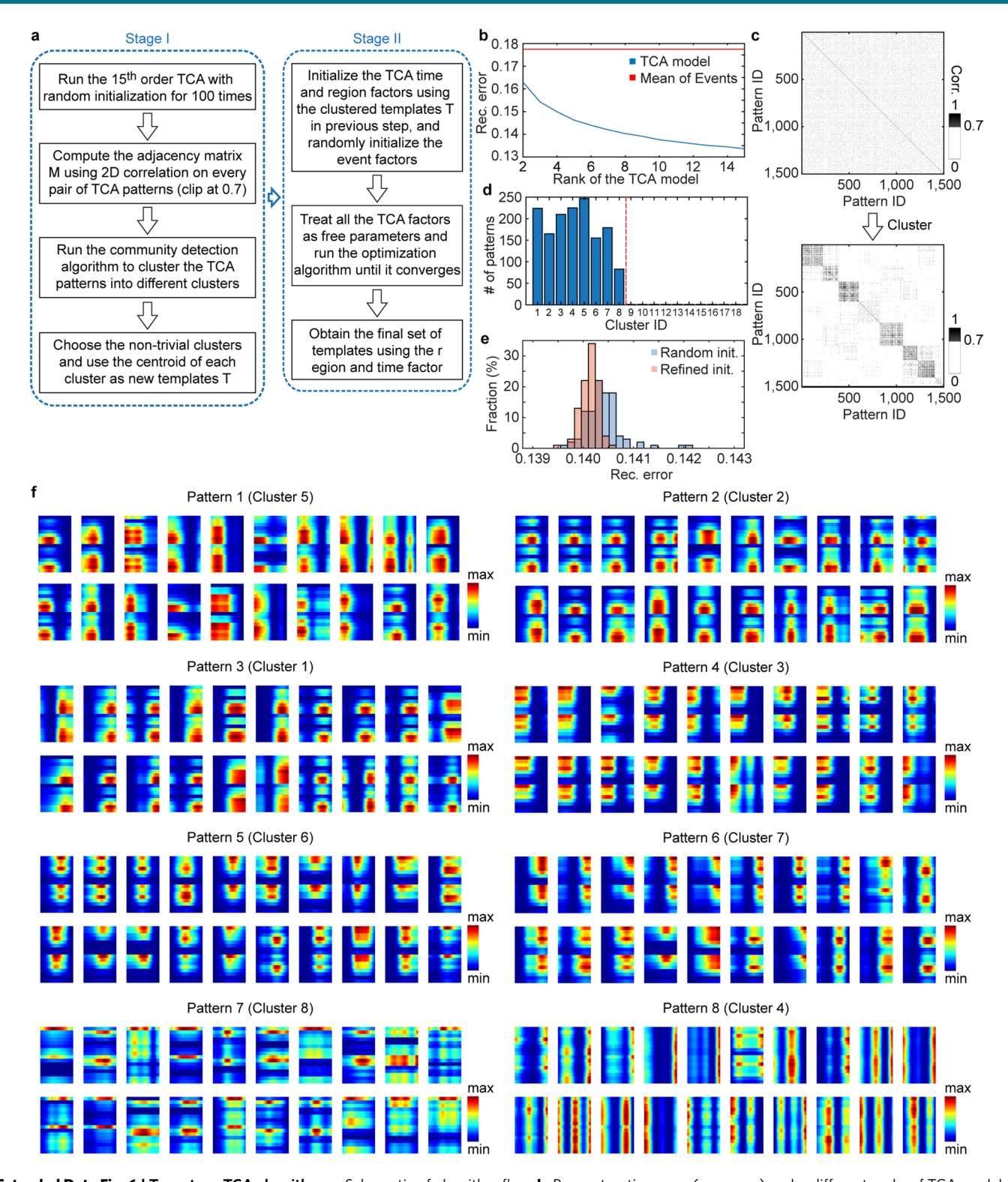
a, Surgical setup of array implantation in actual experiments. Note that the array shank is largely invisible. The edge of the shank is marked by yellow dashed lines. **b**, The staining results of 6 mice, showing the successful penetration to the CA1 pyramidal layer. Arrowheads: trajectory in CA1 pyramidal layer. **c**, The spike waveforms of a few example neurons recorded from different animals. Single neurons can be detected in multiple adjacent channels, each exhibiting different waveform amplitudes.



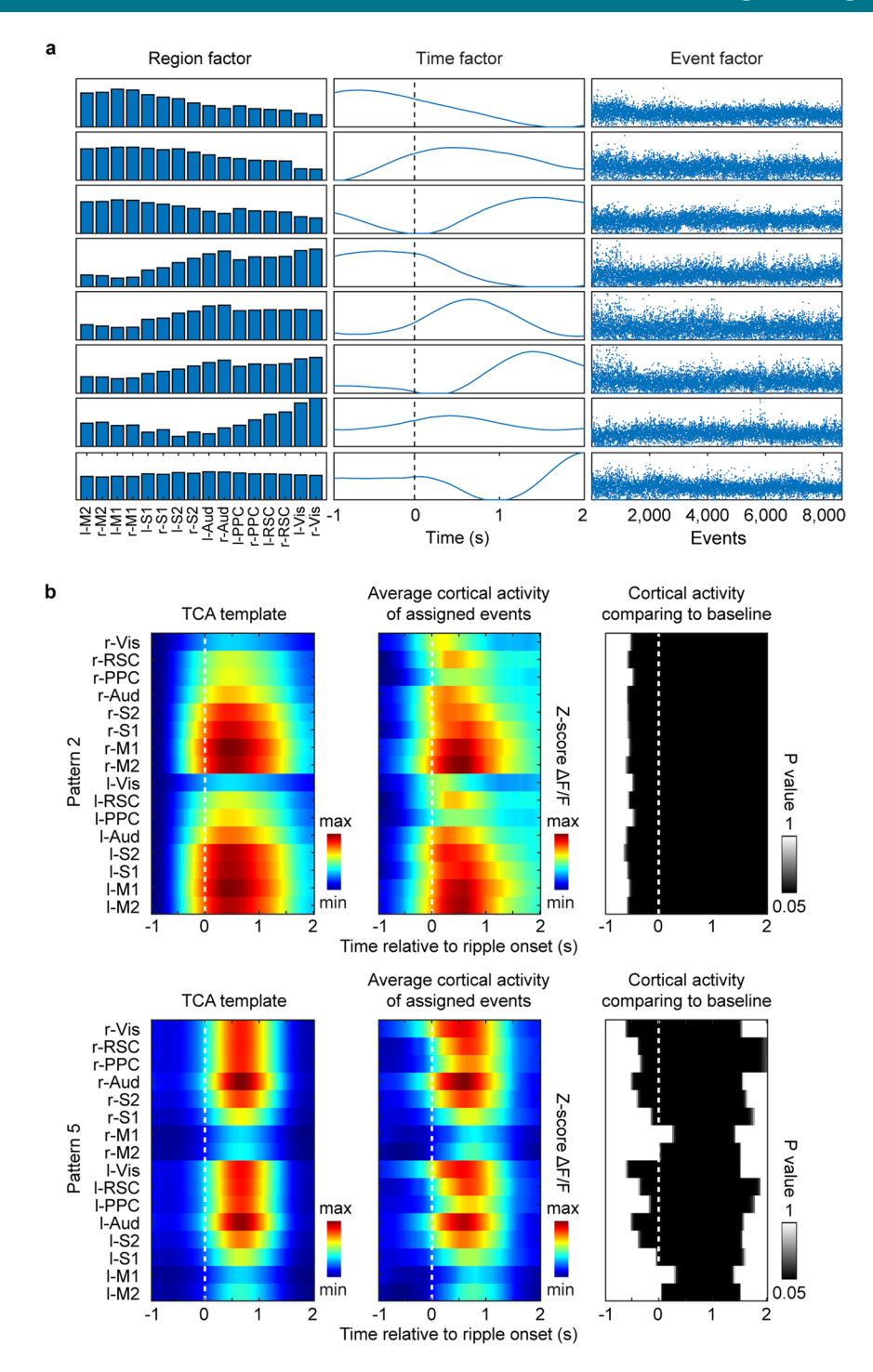
Extended Data Fig. 4 | SWR-associated large-scale cortical activity. a, Averaged cortical activity aligned to SWR onset in each animal. In all animals, the cortex exhibited broad activation around SWRs with the cortical activity rising before SWR onset. **b**, Mean activity in each cortical region aligned to SWR onset (mean ± s.e.m., across SWR events). Black dashed lines: SWR onset.



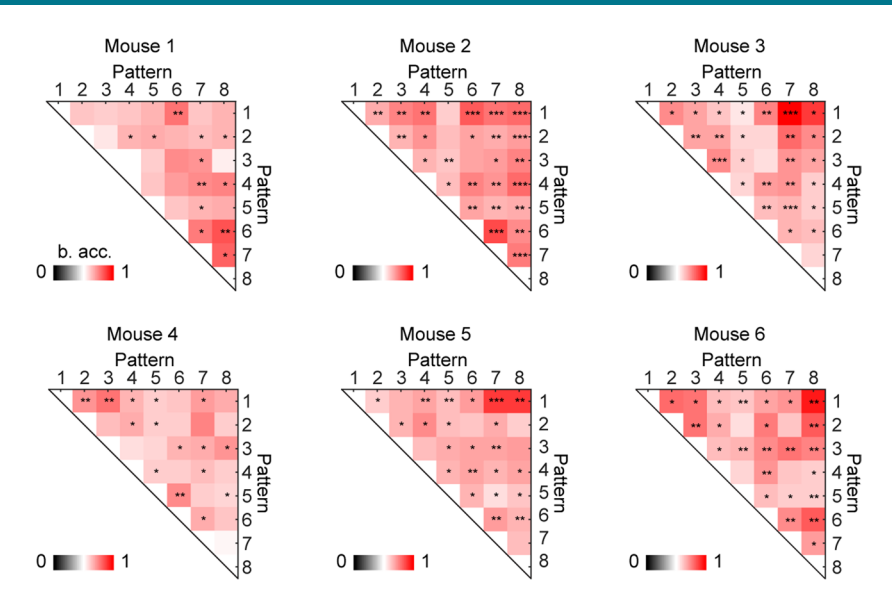
Extended Data Fig. 5 | The distribution of time differences between SWR onset and activity onset in each cortical region. The time differences (SWR onset-cortical activity onset: positive = cortex precedes SWR) formed a continuum around cortical activity onset. Note that the distribution was skewed to positive side in posterior cortical regions, suggesting cortical activity onset in posterior regions preceded SWR onset in a larger fraction of SWR events. Black lines: cortical activity onset.



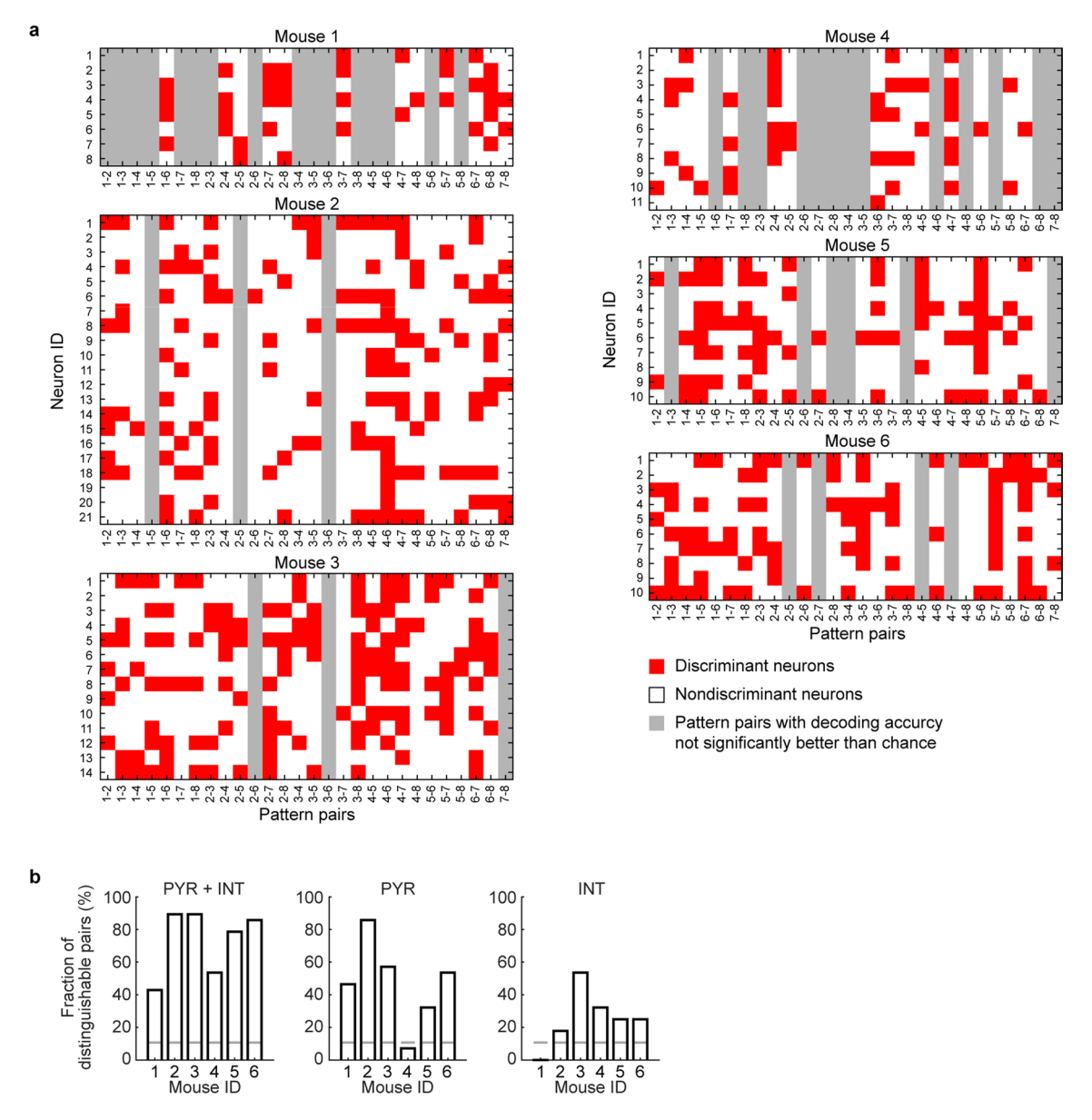
Extended Data Fig. 6 | Two-stage TCA algorithm. a, Schematic of algorithm flow. **b**, Reconstruction error (rec. error) under different ranks of TCA model. **c**, The adjacency matrix before and after clustering. The 1,500 TCA patterns were obtained by the 100 runs of 15th order TCA with random initialization. Corr.: correlation. **d**, Number of assigned patterns in each cluster. Note that only the first 8 clusters had number of assigned patterns > 1. **e**, Reconstruction error (rec. error) of the original TCA algorithm with random initialization and the two-stage TCA algorithm with refined initialization (rank = 8). The reconstruction error given by the two-stage TCA model is smaller than that of the original TCA algorithm with random initialization (two-tailed rank-sum test, $P=1.38\times10^{-11}$, n=100 repetitions for each algorithm), indicating that our two-stage TCA better captured the dynamics of cortical activity. **f**, Randomly selected 20 TCA patterns in each cluster for clusters 1-8. Patterns within each cluster exhibited similar spatiotemporal properties.



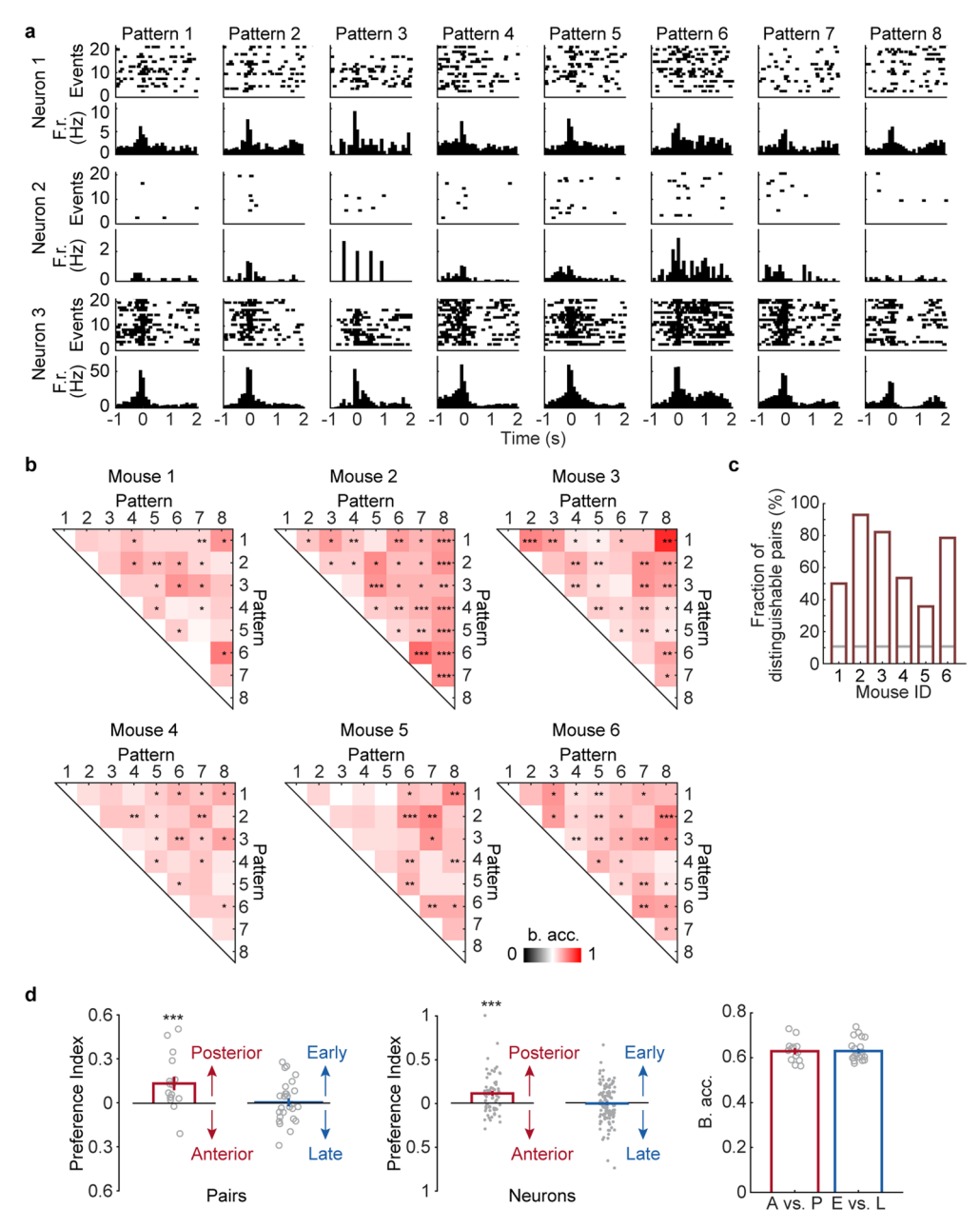
Extended Data Fig. 7 | The two-stage TCA result and the cortical activation timing analysis for two patterns. a, Factors generated by two-stage TCA algorithm. The high-dimensional data of SWR-associated activity from 16 cortical regions was decomposed into 3 factors. The region factors and time factors describe the spatial and temporal dynamics of cortical patterns respectively and the event factors measure the weighting of a given SWR event on the established set of patterns. **b**, Cortical activation timing for pattern 2 and pattern 5. Shown in each row are the pattern template (left), the average cortical activity for the events assigned to the pattern (middle), and the P-value maps (right) for all the cortical regions at [-1 s, 2 s] time interval aligned to SWR onset, showing significantly higher activity than baseline (-1 s) for most cortical regions.



Extended Data Fig. 8 | The decoding accuracy of all cortical pattern pairs in each animal. Many cortical pattern pairs can be distinguished from each other in each animal. The distinguishable pattern pairs are marked by asterisks (shuffling 2,000 times, one-tailed, *P < 0.05, **P < 0.01, ***P < 0.001, see Methods for exact p values). B. acc.: balanced accuracy.



Extended Data Fig. 9 | Discriminant neurons in decoding cortical pattern identity and the fraction of distinguishable pairs using different neuron populations. a, Discriminant neurons selected by feature elimination algorithm in decoding for each pattern pair. Note that the decoding often requires information from multiple hippocampal neurons, and all hippocampal neurons contributed to the decoding of some pattern pairs. **b**, The decoding results of cortical patterns using both the PYR and INT, the PYR only, and the INT only. Gray lines: the chance level fraction with P < 0.05. The chance level number of decodable pattern pairs (nc) was computed from the inverse of binomial cumulative distribution with probability 0.95 (one-sided binomial test, n = 28 pattern pairs). The chance level fraction was obtained by dividing nc with n = 28, the number of pattern pairs on which decoding was performed. PYR: pyramidal neurons, INT: interneurons. For PYR + INT, the p-values for mouse 1-6 are 2.24E-10, 5.10E-32, 5.10E-32, 2.60E-14, 9.17E-26, 8.42E-30. For PYR only, the p-values for mouse 1-6 are 1.26E-11, 8.42E-30, 9.63E-16, 0.16, 5.56E-7, 2.60E-14. For INT only, the p-values for mouse 1-6 are 0.76, 0.0023, 2.60E-14, 5.56E-7, 4.92E-5, 4.92E-5.



Extended Data Fig. 10 | Different cortical activity patterns associated with distinct hippocampal neuronal activity patterns during all SWRs. a, Raster plots (spikes) and the peri-event time histograms of example hippocampal neurons. **b**, Decoding accuracy of all cortical pattern pairs from all 6 animals. Cortical pattern pairs that are significantly distinguishable based on hippocampus activity are marked by asterisks (shuffled 2,000 times, one-tailed, $^*P < 0.05$, $^*P < 0.01$, $^*P < 0.001$, see Methods for exact p values). B. acc.: balanced accuracy. **c**, Fraction of distinguishable cortical pattern pairs in each animal. Gray lines: the chance level fraction with P < 0.05. The p-values for mouse 1-6 are 6.13×10^{-13} , 1.99×10^{-24} , 1.00×10^{-27} , 2.60×10^{-14} , 4.73×10^{-8} , 9.17×10^{-26} , n = 28 pattern pairs. **d**, Preference index and decoding accuracy between anterior (A)-posterior (P) and early (E) - late (L) pattern pairs. Left: preference index of discriminant hippocampus neurons between A-P pairs (pattern 1 vs. 4, 2 vs. 5, and 3 vs. 6) or between E-L patterns (pattern 1 vs. 2, 1 vs. 3, 2 vs. 3, 4 vs. 5, 4 vs. 6, and 5 vs. 6). Posterior patterns were associated with higher firing counts of discriminant neurons than the anterior patterns (two-tailed bootstrap test, 10,000 times, $^{***P}(A-P) = 0.0005$, n = 16 pattern pairs) while no significant differences were detected between early and late patterns (P(E-L) = 0.4380, n = 27 pattern pairs). Gray circles: preference index averaged over all neurons for each pair within each animal. Middle: same as Left but for individual discriminant neurons (two-tailed bootstrap test, 10,000 times, $^{***P}(A-P) = 0$, n = 71 neurons, P(E-L) = 0.3591, n = 129 neurons). Gray dots: preference index of individual discriminant neurons. Right: Decoding accuracy between A-P and E-L pairs was similar (two-tailed bootstrap test, 10,000 times, P = 0.4745, P = 0.

nature research

Corresponding author(s):	Takaki Komiyama and Duygu Kuzum
Last updated by author(s):	Jan 29, 2021

Reporting Summary

Nature Research wishes to improve the reproducibility of the work that we publish. This form provides structure for consistency and transparency in reporting. For further information on Nature Research policies, see our <u>Editorial Policies</u> and the <u>Editorial Policy Checklist</u>.

<u> </u>					
St	ŀа	ŧι	2	ш	\sim

For	all statistical analyses, confirm that the following items are present in the figure legend, table legend, main text, or Methods section.
n/a	Confirmed
	The exact sample size (n) for each experimental group/condition, given as a discrete number and unit of measurement
	A statement on whether measurements were taken from distinct samples or whether the same sample was measured repeatedly
	The statistical test(s) used AND whether they are one- or two-sided Only common tests should be described solely by name; describe more complex techniques in the Methods section.
\boxtimes	A description of all covariates tested
	A description of any assumptions or corrections, such as tests of normality and adjustment for multiple comparisons
	A full description of the statistical parameters including central tendency (e.g. means) or other basic estimates (e.g. regression coefficient AND variation (e.g. standard deviation) or associated estimates of uncertainty (e.g. confidence intervals)
	For null hypothesis testing, the test statistic (e.g. <i>F</i> , <i>t</i> , <i>r</i>) with confidence intervals, effect sizes, degrees of freedom and <i>P</i> value noted <i>Give P values as exact values whenever suitable.</i>
\boxtimes	For Bayesian analysis, information on the choice of priors and Markov chain Monte Carlo settings
\times	For hierarchical and complex designs, identification of the appropriate level for tests and full reporting of outcomes
\times	Estimates of effect sizes (e.g. Cohen's <i>d</i> , Pearson's <i>r</i>), indicating how they were calculated
	Our web collection on <u>statistics for biologists</u> contains articles on many of the points above.

Software and code

Policy information about availability of computer code

Data collection

The electrical recordings was collected by Intan RHD2000 system and loaded into MATLAB for processing using standard script provided by Intan (Version 1.3). The wide-field calcium imaging data was collected by HCImage Live (Hamamatsu) through a commercial fluorescence microscope (Axio Zoom.V16, Zeiss, objective lens (1x, 0.25 NA)) and a CMOS camera (ORCA-Flash4.0 V2, Hamamatsu) and processed using Custom MATLAB code (R2019b).

Data analysis

Custom MATLAB code was used for LFP data processing, ripple detection, statistical analysis and SVM decoding models. The version of the MATLAB program is R2019b. The spike sorting was done with Kilosort v2.0 (https://github.com/MouseLand/Kilosort2). Custom MATLAB code for two-stage TCA algorithm was developed, which requires the tensor toolbox v3.0 for MATLAB (https://www.tensortoolbox.org/) and community detection toolbox (http://netwiki.amath.unc.edu/GenLouvain/GenLouvain). The codes for ripple detection, two-stage tensor component analysis, and the pairwise decoding of cortical patterns are available at https://github.com/xinliuucsd/hippocampus-cortex.

For manuscripts utilizing custom algorithms or software that are central to the research but not yet described in published literature, software must be made available to editors and reviewers. We strongly encourage code deposition in a community repository (e.g. GitHub). See the Nature Research guidelines for submitting code & software for further information.

Data

Policy information about availability of data

All manuscripts must include a data availability statement. This statement should provide the following information, where applicable:

- Accession codes, unique identifiers, or web links for publicly available datasets
- A list of figures that have associated raw data
- A description of any restrictions on data availability

Allen Brain Atlas - Brain Explorer 2: http://mouse.brain-map.org/static/brainexplorer

Figures that have associated raw data: Figures 1-7, Extended Data Figures 3-10. Data available on request from the authors.				
Data available on rec	quest from the authors.			
Field-spe	cific reporting			
•	ne below that is the best fit for your research. If you are not sure, read the appropriate sections before making your selection.			
✓ Life sciences	Behavioural & social sciences Ecological, evolutionary & environmental sciences			
2	he document with all sections, see nature.com/documents/nr-reporting-summary-flat.pdf			
.,				
Life scier	nces study design			
All studies must dis	close on these points even when the disclosure is negative.			
Sample size	No statistical methods were used to predetermine sample size. The animal number was based on previous experiments from our lab (Makino			
	et al., Neuron, 2017) and others using wide-field calcium imaging (Musall et al., Nat. Neurosci, 2019; Pinto et al., Neuron, 2019) and electrophysiological recordings (Clancy et al., Nat. Neurosci, 2019).			
Data exclusions	No animals with successful implantation were excluded from analysis. For all analyses of SWR associated cortical activity except for TCA, we excluded SWR events which had any preceding SWR events within 3 seconds. This was to prevent potential contamination from the tail of			
	cortical activity associated with preceding SWRs. The exclusion criteria were not pre-established.			
Replication	Surgical implantation and recording experiments were repeated in 8 animals. 6 out of 8 replication attempts were successful.			
	No anadomination was affirmed Dandomination is included to a contract of the c			
Randomization	No randomization was performed. Randomization is irrelevant to our study as all animals underwent same surgical and recording procedures.			
Blinding	Investigators were not blind to group allocation during data collection and analysis as all animals underwent same surgical and recording procedures.			
_				
Reportin	g for specific materials, systems and methods			
	on from authors about some types of materials, experimental systems and methods used in many studies. Here, indicate whether each material,			
	ed is relevant to your study. If you are not sure if a list item applies to your research, read the appropriate section before selecting a response.			
	perimental systems Methods			
n/a Involved in th	,			
Antibodies				
Eukaryotic				
	ogy and archaeology MRI-based neuroimaging			
	d other organisms			
	earch participants			
Clinical dat				
Dual use re	esearch of concern			
Antibodies				
Antibodies used	chicken anti-GFP, Aves Labs, AB_2307313			
goat anti-GFAP, Santa Cruz, sc-6170 anti-chicken 488, Jackson Immuno Research, 703-545-155				
	anti-goat 594, Jackson Immuno Research, 703-585-003			
Validation	All the antibodies used in the study have been satisfactorily validated by commercial vendors.			
	chicken anti-GFP, Aves Labs, AB_2307313			
	https://www.aveslabs.com/products/green-fluorescent-protein-gfp-antibody goat anti-GFAP, Santa Cruz, sc-6170			
	https://www.scbt.com/p/gfap-antibody-c-19			
	anti-chicken 488, Jackson Immuno Research, 703-545-155 https://www.jacksonimmuno.com/catalog/products/703-545-155			
	anti-goat 594, Jackson Immuno Research, 703-585-003			
	https://www.jacksonimmuno.com/catalog/products/705-585-003			

Animals and other organisms

Policy information about studies involving animals; ARRIVE guidelines recommended for reporting animal research

Laboratory animals

Mice (cross between CaMKIIa-tTA:B6;CBA-Tg(Camk2a-tTA)1Mmay/J [JAX 003010] and tetO-GCaMP6s: B6;DBA-Tg(tetOGCaMP6s) 2Niell/J [JAX 024742], Jackson laboratories, 6 weeks or older) were group-housed in disposable plastic cages with standard bedding in a room with a reversed light cycle (12 h-12 h). Temperatures and humidity ranged from 18-23 °C and 40-60%, respectively. Experiments were performed during the dark period. Both male and female healthy adult mice were used.

Wild animals

The study did not involve wild animals.

Field-collected samples

The study did not involve samples collected from the field.

Ethics oversight

All procedures were performed in accordance with protocols approved by the UCSD Institutional Animal Care and Use Committee and guidelines of the National Institute of Health.

Note that full information on the approval of the study protocol must also be provided in the manuscript.